Cellular/Molecular

Dendritic Morphology of an Inhibitory Retinal Interneuron Enables Simultaneous Local and Global Synaptic Integration

Espen Hartveit, Margaret Lin Veruki, and Bas-Jan Zandt
Department of Biomedicine, University of Bergen, N-5009 Bergen, Norway

Amacrine cells, inhibitory interneurons of the retina, feature synaptic inputs and outputs in close proximity throughout their dendritic trees, making them notable exceptions to prototypical somato-dendritic integration with output transmitted via axonal action potentials. The extent of dendritic compartmentalization in amacrine cells with widely differing dendritic tree morphology, however, is largely unexplored. Combining compartmental modeling, dendritic Ca^{2+} imaging, targeted microiontophoresis and multielectrode patch-clamp recording (voltage and current clamp, capacitance measurement of exocytosis), we investigated integration in the AII amacrine cell, a narrow-field electrically coupled interneuron that participates in multiple, distinct microcircuits. Physiological experiments were performed with *in vitro* slices prepared from retinas of both male and female rats. We found that the morphology of the AII enables simultaneous local and global integration of inputs targeted to different dendritic regions. Local integration occurs within spatially restricted dendritic subunits and narrow time windows and is largely unaffected by the strength of electrical coupling. In contrast, global integration across the dendritic tree occurs over longer time periods and is markedly influenced by the strength of electrical coupling. These integrative properties enable AII amacrines to combine local control of synaptic plasticity with location-independent global integration. Dynamic inhibitory control of dendritic subunits is likely to be of general importance for amacrine cells, including cells with small dendritic trees, as well as for inhibitory interneurons in other regions of the CNS.

Key words: amacrine cells; dendritic integration; global EPSP; inhibitory interneuron; local EPSP; synaptic integration

Significance Statement

Our understanding of synaptic integration is based on the prototypical morphology of a neuron with multiple dendrites and a single axon at opposing ends of a cell body. Many neurons, notably retinal amacrine cells, are exceptions to this arrangement, and display input and output synapses interspersed along their dendritic branches. In the large dendritic trees of some amacrine cells, such arrangements can give rise to multiple computational subunits. Other amacrine cells, with small dendritic trees, have been assumed to operate as single computational units. Here, we report the surprising result that despite a small dendritic tree, the AII amacrine cell simultaneously performs local integration of synaptic inputs (over smaller dendritic subregions) and global integration across the entire cell.

Introduction

Basic ideas about synaptic integration have been shaped by investigating neurons that display one or more branching dendrites and a single axon emanating from the cell body. In such neurons, integration takes place in the dendritic tree and cell body and output is mediated by action potentials generated in the axon initial segment (Spruston et al., 2016). This view remains important as a framework for understanding axon-carrying neurons, despite growing evidence for the role of dendrites as independent signaling units (Branco and Häusser, 2010). Exceptions to this morphology, however, are considerable (North and Greenspan, 2007; Urban and Margrie, 2016). Particularly notable exceptions are retinal amacrine cells, inhibitory interneurons which feature input and output synapses in close proximity to each other throughout the dendritic tree (Masland, 2012; Helmstaedter et al., 2013). These synapses establish a variety of microcircuit arrangements as substrates for neuronal computations (Fain, 1981; Diamond, 2017). Amacrine cells display extreme heterogeneity (~60 types based on molecular phenotyping; Yan et al., 2020) and each type has a characteristic morphology, dendritic branching pattern, stratification in the inner plexiform layer (IPL), and arrangement of synapses (Masland, 2012; Diamond, 2017). Like inhibitory interneurons elsewhere in the CNS, amacrine cells are thought to contribute to signal processing by transforming and shaping the

Received Apr. 1, 2021; revised Dec. 21, 2021; accepted Dec. 23, 2021.

Author contributions: E.H. designed research; E.H., M.L.V., and B.-J.Z. performed research; E.H., M.L.V., and B.-J.Z. analyzed data; E.H. wrote the first draft of the paper; E.H., M.L.V., and B.-J.Z. edited the paper; E.H., M.L.V., and B.-J.Z. wrote the paper.

This work was supported by the Research Council of Norway Grants 214216 (to E.H.) and 261914 (to M.L.V.).

The authors declare no competing financial interests.

Correspondence should be addressed to Espen Hartveit at espen.hartveit@biomed.uib.no.

https://doi.org/10.1523/JNEUROSCI.0695-21.2021

responses of other neurons. Wide-field amacrines (e.g., A17 and starburst) have large and extensive dendritic trees, with limited communication between different regions (Euler et al., 2002; Grimes et al., 2009, 2010; Koren et al., 2017; Poleg-Polsky et al., 2018). In these neurons, processing and integration of synaptic potentials is primarily local, mediated by various combinations of electrotonic compartmentalization and active membrane properties. In this way, signals in different subunits of the dendritic tree are processed in relative isolation. Other amacrine cells, referred to as narrow-field, typically send processes into both sublamina *a* and *b* of the IPL, enabling them to receive excitatory input from bipolar cells with opposite response polarities (ON vs OFF). Through inputs and outputs in functionally opposing layers, narrow-field amacrines could mediate vertical interactions across the IPL, including interactions between the ON and OFF pathways (Roska and Werblin, 2001), with greater separation between inputs and outputs. Alternatively, these cells may primarily participate in multiple distinct microcircuits with local integration and signal processing (e.g., the vGluT3 amacrine; Chen et al., 2017; Hsiang et al., 2017).

The bistratified AII is the best characterized of such narrow-field, multifunctional amacrine cells and is connected to a large number of different neurons (Marc et al., 2014). At proximal and distal dendritic regions (in different sublaminae of the IPL), the AII receives glutamatergic excitation from different types of bipolar cells and at proximal dendrites it provides glycinergic inhibition to OFF-cone bipolar and ganglion cells. Distal dendrites are also connected via electrical synapses to other AIIs and ON-cone bipolar cells (Pourcho and Goebel, 1985; Strettoi et al., 1990, 1992, 1994; Chun et al., 1993; Veruki and Hartveit, 2002a, b; Singer and Diamond, 2003; Veruki et al., 2003; Graydon et al., 2018; Hartveit et al., 2019). This morphologically segregated connectivity raises the question whether synaptic integration in AIIs is predominantly local (with functionally independent microcircuits) or whether there is consequential global integration encompassing the entire dendritic tree. Remarkably, there is no direct evidence for vertical signal transmission between proximal and distal dendritic regions of the AII. Like many inhibitory interneurons (Abrahamsson et al., 2012; Tran-Van-Minh et al., 2016), AIIs have very thin dendrites (Tsukamoto and Omi, 2013) that are probably too thin for patch-clamp recording (Hu et al., 2010; Vervaeke et al., 2012). Instead, we have combined morphologically realistic, conductance-based computational modeling, Ca^{2+} imaging, and multielectrode whole-cell recording to investigate dendritic integration in AII amacrine cells. We provide direct evidence for vertical transmission that links inputs and outputs at opposite regions of the dendritic tree and discovered that the dendritic morphology enables simultaneous local and global integration.

Materials and Methods

Retinal slice preparation

The use of animals in this study was conducted under the approval of and in accordance with the regulations of the Animal Laboratory Facility at the Faculty of Medicine at the University of Bergen (accredited by AAALAC International). Albino rats (four to seven weeks postnatal, male and female) had *ad libitum* access to food and water and were kept on a 12/12 h light/dark cycle. Animals were deeply anaesthetized with isoflurane in oxygen and killed by cervical dislocation. Retinal slices were cut by hand with a curved scalpel blade at a thickness of ~100 to ~150 µm. Experiments were performed at two different setups. One setup used a custom-modified Movable Objective Microscope (MOM; Sutter Instrument; RRID:SCR_018860) with a 20× water immersion objective (XLUMPLFL; 0.95 NA; Olympus) and infrared Dodt gradient contrast videomicroscopy (IR-DGC; Luigs & Neumann; Dodt et al., 1998), using an IR-sensitive analog CCD camera (VX55; TILL Photonics). The cell bodies of the recorded cells were generally located 20–30 µm below the surface of the slice. A second setup was equipped with an upright microscope (BX51WI) with a 40× (0.8 NA) or a 60× (0.9 NA; Olympus) water immersion objective and infrared differential interference contrast (IR-DIC) videomicroscopy. Electrophysiological recording and imaging were conducted at room temperature and for each experiment the temperature was monitored continuously at the recording chamber. The average temperature was 25°C, but ranged between 21°C and 27°C (across all experiments reported here). The fluctuation within the recording period of a single cell was typically ±0.1°C.

Solutions and drugs

The extracellular perfusing solution was continuously bubbled with 95% O_2/5% CO_2 and had the following composition: 125 mM NaCl, 25 mM $NaHCO_3$, 2.5 mM KCl, 2.5 mM $CaCl_2$, 1 mM $MgCl_2$, and 10 mM glucose, pH 7.4 (osmolality ~300 mOsm kg^{-1} H_2O). A series of intracellular solutions were used; in the figures, these are referred to by a capital letter (A–F) and by their main constituent (K-gluconate in A, B, D, and F; KCl in C; and $CsCH_3SO_3$ in E). For multiphoton excitation (MPE) microscopy and imaging of intracellular Ca^{2+} in AII amacrine cells, the recording pipettes were filled with intracellular solution A of the following composition: 125 mM K-gluconate, 5 mM KCl, 8 mM NaCl, 10 mM HEPES, 4 mM MgATP, and 0.4 mM Na_3GTP (pH adjusted to 7.3 with KOH). The solution also contained 200 µM Oregon Green 488 BAPTA-1 (OGB-1; Invitrogen/Thermo Fisher Scientific) and 40 µM Alexa Fluor 594 hydrazide as sodium salt (Alexa 594; Invitrogen/Thermo Fisher Scientific). For triple recordings of an AII amacrine cell and two bipolar cells, the AII recording pipette was filled with intracellular solution B of the following composition: 125 mM K-gluconate, 8 mM NaCl, 1 mM $CaCl_2$, 5 mM EGTA, 10 mM HEPES, 4 mM MgATP, and 2 mM N-(2, 6-dimethylphenylcarbamoylmethyl)triethyl-ammonium bromide (QX314; pH adjusted to 7.3 with KOH). The solution also contained 100 µM Alexa Fluor 488 hydrazide as sodium salt (Alexa 488; Invitrogen/Thermo Fisher Scientific). The bipolar cell pipette solution C contained the following: 130 mM KCl, 8 mM NaCl, 10 mM HEPES, 1 mM $CaCl_2$, 5 mM EGTA, and 4 mM MgATP (pH adjusted to 7.3 with KOH). The alternative bipolar cell pipette solution D contained the following: 125 mM K-gluconate, 8 mM NaCl, 1 mM $CaCl_2$, 5 mM EGTA, 10 mM HEPES, and 4 mM MgATP (pH adjusted to 7.3 with KOH). Both bipolar cell solutions also contained 40 or 50 µM Alexa 594. For capacitance measurements in single recordings of AII amacrine cells, we used pipette solution E which contained the following: 80 mM Cs-methanesulfonate ($CsCH_3SO_3$), 40 mM CsCl, 10 mM tetraethylammonium chloride (TEA-Cl), 28 mM HEPES, 2 mM EGTA, 3 mM MgATP, 1 mM Na_3GTP, and 0.04 mM Alexa 594 (pH adjusted to 7.3 with CsOH). For capacitance measurements in dual recordings of rod bipolar and AII amacrine cells, pipette solution F for the rod bipolar cell contained the following: 125 mM K-gluconate, 5 mM KCl, 8 mM NaCl, 10 mM HEPES, 0.2 mM EGTA, 4 mM MgATP, 0.4 mM Na_3GTP, and 0.04 mM Alexa 594 (pH adjusted to 7.3 with KOH). The pipette solution for the AII amacrine cell was identical to that used for AIIs in triple recordings (B; see above). For all intracellular solutions, the osmolality was ~290 mOsm kg^{-1} H_2O. The data acquisition software (Patchmaster; HEKA Elektronik; RRID:SCR_000034) corrected all holding potentials for liquid junction potentials on-line. Theoretical liquid junction potentials were calculated with JPCalcW (Molecular Devices). In some experiments, drugs were added to the extracellular solution used to perfuse the slices. The concentrations of drugs were as follows (supplier Tocris Bioscience, unless otherwise noted): 10 µM bicuculline methchloride (to block $GABA_A$ receptors), 10 µM 6-cyano-7-nitroquinoxaline-2,3-dione (CNQX; to block non-NMDA glutamate receptors), 1 µM strychnine (to block glycine receptors; Research Biochemicals International), 20 µM 3-((*RS*)−2-carboxypiperazin-4-yl)-propyl-1-phosphonic acid (CPP; to block NMDA glutamate receptors), and 1 µM tetrodotoxin (TTX; to block voltage-gated Na^+ channels). The solutions were prepared from concentrated aliquots stored at −20°C.

Electrophysiological recording and data acquisition

Patch pipettes were pulled from thick-walled borosilicate glass (outer diameter, 1.5 mm; inner diameter, 0.86 mm). The open-tip resistance of

the pipettes ranged between ~5 and ~10 MΩ when filled with intracellular solution. Whole-cell voltage-clamp and current-clamp recordings from AII amacrine cells and rod and cone bipolar cells were performed with either an EPC10-triple, an EPC10-USB-dual or an EPC10-USB-quadro amplifier (HEKA Elektronik) controlled by Patchmaster software. When establishing a recording, leakage of dye from the recording pipette was minimized to reduce the background fluorescence around the cell body. After establishing GΩ-seals (≥2 GΩ), currents caused by the recording electrode capacitance were automatically measured and neutralized by the amplifier (C_{fast} function of Patchmaster software). After breaking into a cell, currents caused by the cell membrane capacitance were partially neutralized by the amplifier (C_{slow} function of Patchmaster software). When we sampled current responses for capacitance measurement of depolarization-evoked exocytosis, the C_{slow} capacitance neutralization circuitry was always enabled. In voltage-clamp recordings, the cells were held at a potential (V_{hold}) of −60 mV (unless otherwise stated). Signals were low-pass filtered (analog three-pole and four-pole Bessel filters in series) with a corner frequency (−3 dB) set to 1/5 of the inverse of the sampling interval (50–100 µs, depending on protocol).

To stabilize the membrane potential in current-clamp recordings, we used the low-frequency voltage-clamp (LFVC) function (Peters et al., 2000) of the Patchmaster/EPC10 instrumentation for the AII amacrine recordings. The potential was set to −60 mV and the time constant was set to ~30 s (for details, see Zandt et al., 2018). Before switching to current clamp, pipette capacitance and series resistance were estimated (and pipette capacitance compensated) in voltage-clamp mode. After switching to current clamp, series resistance compensation (bridge balance) was checked manually and adjusted when required. This was repeated regularly throughout a recording.

Capacitance measurements of exocytosis from AII amacrine cells

Capacitance measurements were obtained with the "Sine + DC" lock-in technique (Lindau and Neher, 1988; Gillis, 1995) as implemented in Patchmaster software in combination with the EPC10-triple amplifier. To reduce the effective capacitance of the recording pipettes, they were coated with Parafilm (American National Can) and the fluid levels in the recording chamber and pipette were kept low. For experiments designed to measure a potential increase of capacitance evoked by exocytosis, we used a fixed sine wave frequency of 1 or 2 kHz and peak amplitude of ±20 mV relative to V_{hold} = −90 mV (Balakrishnan et al., 2015; for a detailed theoretical and experimental analysis, see Hartveit et al., 2019). The current signal was low-pass filtered (analog three-pole and four-pole Bessel filters in series) with a cutoff frequency of 2× the sine wave frequency and sampled at a frequency of 10× the sine wave frequency. After sampling, the current signal was processed by the lock-in extension of Patchmaster to obtain estimates of total membrane capacitance (c_m), total membrane conductance (g; inverse of total membrane resistance r_m) and series conductance (G_s; inverse of series resistance R_s), with a temporal resolution of one data point per sine wave cycle. For subsequent analysis, we averaged the results from 10 such sine wave cycle data points and low-pass filtered the obtained waveform at 10 or 20 Hz. For measurements of depolarization-evoked exocytosis, the phase shift and attenuation of the measuring system was calibrated with the "calculated" method in Patchmaster software.

Stimulus-evoked changes in c_m (Δc_m) were calculated as the difference between the average during a 100- to 1000-ms period before and after the stimulus. Two different stimulus paradigms were applied with the goal of evoking exocytosis from AII amacrine cells. In the first paradigm, we recorded an EPSP in an AII amacrine cell evoked by depolarization of a rod bipolar cell during a dual recording of two synaptically connected cells. The EPSP waveform was then applied as a voltage-clamp command template to other AII amacrine cells and the capacitance was measured before and after the depolarization (as described above) without interrupting the acquisition. These recordings were performed with a Cs^+-based intracellular solution (E). In the second paradigm, we performed simultaneous, dual recordings from synaptically connected rod bipolar cells and AII amacrine cells. First, the baseline capacitance of the AII amacrine cell was measured in voltage clamp (V_{hold} = −90 mV). After changing V_{hold} to −60 mV, the acquisition was briefly interrupted (for ~600 ms) and the recording configuration was switched from voltage to current clamp, using the "gentle switch" function of the EPC10/Patchmaster instrumentation to keep the membrane potential at approximately −60 mV. Next, with the AII amacrine in current clamp, the rod bipolar cell (in voltage clamp) was depolarized from −60 to −20 mV (for 100 ms) to evoke exocytosis from this cell. At the end of the voltage command, the AII amacrine cell was switched from current clamp to voltage clamp (V_{hold} = −90 mV), using the "rapid mode switch" function of the EPC10/Patchmaster instrumentation during continued acquisition. After 100 ms at V_{hold} = −90 mV, we applied a second sine wave stimulus to measure the capacitance of the AII amacrine cell (V_{hold} = −90 mV). Between each measurement cycle, the AII was held in voltage clamp at −60 mV. These recordings were performed with K^+-based intracellular solutions in both the rod bipolar (F) and AII amacrine cell (B). The intracellular solution for the AII also contained QX314 to block voltage-gated Na^+ channels. For both paradigms, stimuli to evoke exocytosis were applied at intervals of ~60 s. For capacitance measurements in single recordings of AII amacrines, the bath solution contained drugs to block voltage-gated Na^+ channels and $GABA_A$, glycine, non-NMDA, and NMDA glutamate receptors.

Ultrafast microiontophoretic application of glutamate

In some experiments we used high-resolution, ultrafast microiontophoresis to activate glutamate receptors on AII amacrine cells (Castilho et al., 2015). High-resistance pipettes (90–100 MΩ) were pulled (P-97; Sutter Instrument) from filamented borosilicate glass (outer diameter, 1.5 mm; inner diameter, 0.86 mm) and filled with 150 mM glutamate (pH adjusted to 7.4 with NaOH). Alexa 594 (50 µM) was added for visualization of the pipette tip. The pipette capacitance was compensated by the microiontophoresis amplifier (MVCS-C-02M; NPI Electronic). Brief (1 ms), negative current pulses (−25 to −500 nA) were applied to eject glutamate after the pipette was positioned close (~2 µm) to a varicosity of an AII arboreal or a lobular dendrite under visual control using MPE microscopy (for additional details, see Hartveit and Veruki, 2019). When combined with Ca^{2+} imaging (see below), the stimulus interval was ≥30 s. For microiontophoresis experiments, the bath solution contained TTX to block voltage-gated Na^+ channels (except when such channel activity disappeared while waiting for the cell to fill with fluorescent dyes; see below).

MPE fluorescence microscopy and Ca^{2+} imaging

Red (from Alexa 594) and green (from OGB-1) fluorescence for structural and functional (Ca^{2+}) imaging, respectively, were imaged with the MOM equipped with a Ti:sapphire laser (Mai Tai DeepSee; Spectra-Physics) tuned to 810 nm. Analog signals were digitized by an acquisition board (PXIe-6356, National Instruments) and MPE microscopy and image acquisition were controlled by ScanImage software (version 2018bR1; Vidrio Technologies; RRID:SCR_014307) running under Matlab (The Mathworks; RRID:SCR_001622). For cellular morphology, image stacks were acquired as a series of optical sections (1024 × 1024 pixels) with XY pixel size ~70 to ~80 nm (depending on the magnitude of the digital zoom factor) and collected at a focal plane interval of 0.4 µm, sufficient to satisfy Nyquist rate sampling (for details, see Zandt et al., 2017, 2018).

For imaging intracellular Ca^{2+} dynamics in processes of AII amacrine cells, we sampled red and green fluorescence at constant focal planes in frame-scan mode (temporal resolution 16–50 Hz), using the multiple region of interest (MROI) imaging functionality of ScanImage to selectively image at multiple, discrete locations within a single frame-scan acquisition cycle. Each individual ROI was typically between 24 × 24 and 70 × 70 pixels (0.2–0.5 µm/pixel) and within each frame we typically acquired three to eight individual ROIs. Ca^{2+} imaging started at least 10–15 min after establishing the whole-cell configuration to allow for maximal indicator loading at the distal AII arboreal dendrites in stratum 5 (S5) of the IPL.

Frame-scan imaging data were analyzed in IGOR Pro. Background fluorescence (F_b) was measured as the average signal from a rectangular area close to the ROI (but without contamination from dye spilled

extracellularly when the whole-cell recording was established). Baseline fluorescence (F_0) was measured by averaging the signal during an interval (typically 0.5–1 s) before stimulus onset. For a given signal (F), the relative change in fluorescence related to a change in Ca^{2+} was calculated as follows (Yasuda et al., 2004):

$$\frac{\Delta F}{F_0} = \frac{F - F_0}{F_0 - F_b}, \quad (1)$$

and for simplicity referred to as $\Delta F/F$. In addition, we also calculated the ratio of green fluorescence (G) over red fluorescence (R), and measured changes in Ca^{2+} as the difference between G/R for a given point in time and G/R averaged for the baseline period. For simplicity, this measure is referred to as $\Delta G/R$. For the relatively brief periods employed for each frame-scan period (~6 s), $\Delta G/R$ was essentially identical to $\Delta F/F$ and only the latter analysis will be reported here. The $\Delta F/F$ data were digitally filtered with a boxcar (sliding average) smoothing function (IGOR Pro, WaveMetrics; RRID:SCR_000325). Filtered $\Delta F/F$ responses were analyzed by curve fitting with a triple-exponential function with two decay components (Fernández-Alfonso et al., 2014):

$$F(t) = (1 - exp(-(t - t_0)/\tau_r))^N \times (A_1 exp(-(t - t_0)/\tau_1) + A_2 exp(-(t - t_0)/\tau_2)), \quad (2)$$

where $F(t)$ is the fluorescence ($\Delta F/F$) as a function of time, t_0 is the time of onset, τ_r is the time constant of the rising phase, A_1 and A_2 are the amplitudes, τ_1 and τ_2 are the corresponding time constants of decay, and the exponent N smooths the transition from the baseline to the onset of the response.

3D morphologic reconstruction

Quantitative morphologic reconstruction of fluorescently labeled AII amacrine cells imaged by MPE microscopy was done manually using computer-guided neuronal tracing software (Neurolucida 360, v2019, 64-bit; MBF Bioscience; RRID:SCR_016788). Before reconstruction, image stacks were deconvolved (Huygens Essential, v19 64-bit; Scientific Volume Imaging; RRID:SCR_014237) to remove noise and reassign out-of-focus light with a theoretically calculated point spread function (for details, see Zandt et al., 2017). Reconstruction of the soma was performed by tracing it with a single contour corresponding to the focal plane with the largest soma profile. As reconstructions were based on live cell imaging, no correction for errors related to shrinkage was necessary.

Wide-field fluorescence microscopy

In the recordings for capacitance measurements and tests of synaptic connectivity, wide-field fluorescence microscopy was used to acquire image stacks of neurons filled with fluorescent dye, using a TILLvisION system (TILL Photonics). An image stack was acquired as a series of optical sections collected at temporal intervals of ~500 ms and focal plane intervals of 0.5 µm, using a cooled, interline transfer CCD camera (Imago QE). The excitation light source (Polychrome V) was coupled to the epifluorescence port of the microscope with a custom-made condenser via a quartz fiber-optic light guide. The wavelength of the excitation light was 570 nm, and the exposure time was 50–100 ms. At the total magnification used, the pixel size (X, Y) was ~107 and ~163 nm for the 60× and 40× objectives, respectively. For imaging Alexa 594 fluorescence, the mirror unit consisted of an excitation filter (ET560/40×), a dichroic mirror (T590LPXR), and an emission filter (ET590LP). For imaging Alexa 488 fluorescence, the mirror unit consisted of an excitation filter (ET480/40×), a dichroic mirror (T510LPXRXT), and an emission filter (ET510LP). All filters were purchased from Chroma. After acquisition, Huygens Essential was used for deconvolution. Maximum intensity projections were generated with Huygens Essential. Final adjustments of contrast, brightness, levels, and γ were applied homogeneously across the entire image.

Computer modeling and simulation

Computer simulations of compartmental models were performed with NEURON (versions 7.3 and 7.4; RRID:SCR_005393) running under Mac OS X (10.9.5). All models used for simulations in the current study were developed in a previous study from our laboratory (Zandt et al., 2018). These models were developed from correlated morphologic reconstructions and physiological measurements, with the best-fitting passive membrane properties (cytoplasmic resistivity, R_i; specific membrane capacitance, C_m; and specific membrane resistance, R_m) determined for each cell (cf. Major, 2001; Holmes, 2010). For additional details, including the best-fit passive membrane parameters of the cells, see Zandt et al. (2018). Simulations of single neurons were run with a fixed time step of 10 or 25 µs or, alternatively, with a variable time step and the absolute tolerance set to 0.001. For control, some simulations were repeated after reducing the time step to 1 µs or the absolute tolerance to 0.0001 or 0.00001, but the results did not change appreciably (<~1%). For simulations of networks of neurons with electrical coupling (simulating the effect of gap junction coupling), we mostly used a fixed time step of 5 µs. In all simulations, spatial discretization (compartmentalization) was implemented by applying the *d_lambda* rule (Carnevale and Hines, 2006). Briefly, the alternating current (AC) length constant at 100 Hz (λ_{100}) was calculated for each section (branch segment, i.e., a continuous length of unbranched cable) and the number of segments (*nseg*) in each section was adjusted such that the length of each segment was smaller than a fraction *d_lambda* of λ_{100}, with *d_lambda* set to 0.1. In a few simulations, *d_lambda* was reduced to 0.01, but this did not appreciably change the results. The segment lengths were calculated using NEURON's standard values for C_m, R_m, and R_i (1.0 µF cm^{-2}, 1000 Ω cm^2, and 35.4 Ω cm, respectively). This resulted in almost all sections being modeled with a single compartment. Corresponding to this, the average number of sections was 390 ± 120 (SD; range = 210–624) and the average number of segments was 400 ± 110 (SD; range = 213–635; $n = 13$ cells with morphologic reconstruction and compartmental models). In the simulations, an idealized single-electrode current clamp (IClamp; from the standard repertoire of NEURON point processes) was connected to the soma compartment.

A synapse was implemented as a point process in NEURON, locally generating a current $I_{syn}(t) = g_{syn}(t) \times [V_m(t) - E_{syn}]$, where $g_{syn}(t)$ is the predefined synaptic conductance waveform (see below), $V_m(t)$ is the postsynaptic membrane potential (as a function of time), and E_{syn} is the synaptic reversal potential. Before each simulation run, the model was initialized to steady-state (Carnevale and Hines, 2006). For quantitative analysis of signal transmission between different cellular compartments, all 13 cells were used. The reversal potential (E_{rev}) of the leak current (e_pas) was set to −60 mV (the holding potential used during acquisition of experimental traces), except for some simulations where it was set to −50 mV (as indicated in the text).

Synaptic conductance waveforms injected into the theoretical computer models were modeled as an error function multiplied with an exponential decay (Zandt et al., 2018):

$$\begin{aligned} g_{syn}(t) &= g_0 \times a[(1 + erf((t - \delta)/\tau_{rise} - 2)) \times exp(-(t - \delta)/\tau_{decay})] && \text{for } t \geq 0 \\ g_{syn}(t) &= 0 && \text{for } t < 0 \end{aligned}, \quad (3)$$

where g_0 is the peak conductance, δ is the delay to onset, τ_{rise} is the rise time constant, *erf* is the error function, τ_{decay} is the decay time constant, and a is a scaling factor to scale the peak of the expression within the square parenthesis to 1. We found that this waveform closely reproduced the shape of experimentally recorded spontaneous EPSCs (spEPSCs) in AII amacrine cells (Veruki et al., 2003). At room temperature, spEPSCs in these cells have an average 10–90% rise time of ~340 µs, decay time constant of ~760 µs (when fitted with a single exponential), and peak amplitude of ~29 pA (at V_{hold} = −60 mV; Veruki et al., 2003). An average spEPSC obtained from a single cell with properties close to the population average was selected and the parameters of Equation 3 were fitted to closely reproduce this spEPSC. In this way, we obtained g_0 = 480 pS (corresponding to a 29-pA current for a 60-mV driving force), τ_{rise} =

224 µs (corresponding to a 10–90% rise time of 340 µs), and τ_{decay} = 760 µs. The reversal potential of g_{syn} was set to 0 mV (E_{syn} = 0 mV). Because there is no experimental evidence for any systematic regional nonuniformity of kinetics and/or amplitude of EPSCs, the same parameters were used for simulating synaptic inputs across the dendritic tree, corresponding to putative input from rod bipolar cells and OFF-cone bipolar cells at the arboreal and lobular dendrites, respectively. To implement electrical coupling of the AII compartmental models, we placed identical copies of the same cell in a hexagonal network and linked each cell to all of its nearest (directly connected) neighbors, as described in Hartveit et al. (2019).

Experimental design, statistical analysis, and data presentation

Data were analyzed with NEURON and IGOR Pro. Data are presented as means ± SD (n = number of cells). Statistical analysis was performed using Student's two-tailed t test (paired). Differences were considered statistically significant at the $p < 0.05$ level. The number of individual traces included in the averaged current or voltage traces in the figures are stated for each case. For illustration purposes, most raw records (current or voltage) were low-pass filtered (digital Gaussian filter, −3 dB at 500 Hz to 1 kHz) or smoothed by a binomial smoothing function (IGOR Pro) to emphasize the kinetics of the response.

Results

Compartmental modeling reveals location-dependent synaptic signaling in AII amacrine cells

To investigate dendritic signaling in AIIs, we explored the magnitude and spatial extent of the responses evoked by excitatory synaptic inputs at different locations (Fig. 1). We used experimentally constrained compartmental models of AII amacrines, developed from combined electrophysiological recording and quantitative morphologic reconstruction (Zandt et al., 2018). Synaptic input was implemented by injecting a conductance waveform (g_{syn}; Fig. 1*A*), modeled after spEPSCs in AII amacrines (Veruki et al., 2003).

The synaptic location strongly influenced the local EPSPs. With a single g_{syn} event injected at the tip of an arboreal dendrite (Fig. 1*B*), the local EPSP (7–8 mV) was much larger than the soma EPSP (~1.5 mV). In contrast, with g_{syn} applied close to the apical dendrite (Fig. 1*C*), the local EPSP (~1.9 mV) was much smaller and very similar to the soma EPSP (~1.6 mV). For both stimulus locations, the most pronounced difference between the local and soma EPSPs was observed during the period of increased conductance, when the local membrane potential rapidly equilibrated with that at the soma. The local and soma EPSPs equalized within ~5 ms after stimulus onset, following which the membrane potential decayed exponentially, according to the value of the membrane time constant (37 ms; cf. Zandt et al., 2018; Fig. 1*B*,*C*). The larger amplitude and fast kinetics of the local EPSP at the arboreal dendrite can be attributed to the high local input resistance and fast intracellular charge redistribution. With higher-frequency synaptic input (15 g_{syn} events at 100 Hz) at the same location, the local summation followed a time course identical to the summation at the soma, with brief, local depolarizations riding on top of the slow, common depolarization (Fig. 1*B*,*C*). At dendritic locations far from the synaptic input, the

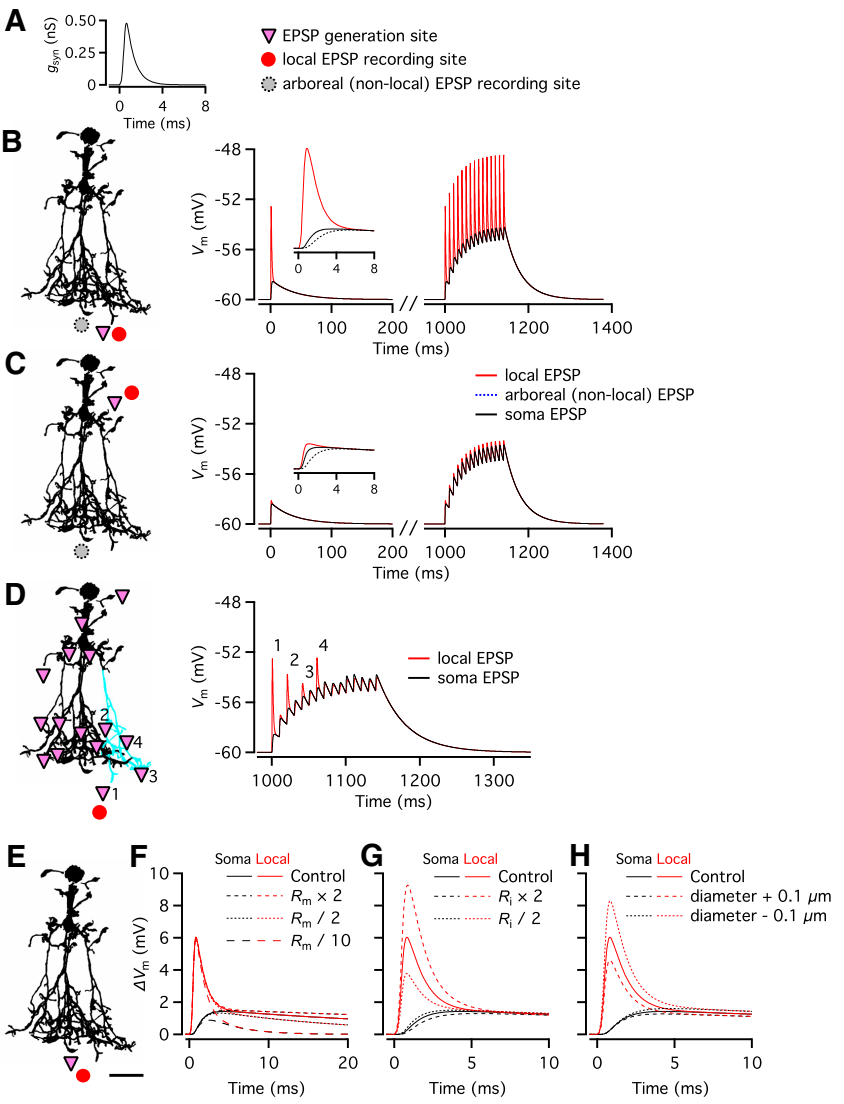

Figure 1. Location-dependent synaptic signaling in AII amacrines. ***A***, Quantal synaptic conductance waveform (g_{syn}) used for compartmental model simulations. ***B***, Voltage responses of AII (shape plot of morphologic reconstruction at left) evoked by injecting g_{syn} at arboreal dendrite (triangle). EPSP recorded at generation site (red circle; local EPSP; red lines), neighboring dendrite (dashed circle; nonlocal EPSP; dashed black lines) and soma (soma EPSP; continuous black lines). Here and later, soma EPSP superimposed on other membrane potentials. Response evoked by single stimulus (expanded time scale in inset) or by 15 stimuli (10-ms interval; same location). ***C***, As ***B***, but g_{syn} injected at lobular appendage (triangle). ***D***, Integration of synaptic inputs at 15 locations (triangles; 10-ms intervals). Sites 1–4 in same subtree (blue). EPSPs recorded at synaptic site 1 (red circle; local EPSP, red line) and soma (black line). ***E–H***, Influence of passive membrane properties and morphology on kinetics and amplitude characteristics of local and global EPSPs. ***E***, Shape plot of AII used for compartmental modeling (***F–H***). Quantal synaptic conductance waveform (g_{syn}; as in ***A***) injected at distal tip of arboreal dendrite (marked by triangle). Local EPSP recorded at same location (marked by red circle). ***F–H***, Local (red traces) and soma (black traces) EPSPs recorded for control and modified values of specific membrane resistance (R_m; ***F***), cytoplasmic resistivity (R_i; ***G***), and process diameter (d; with no diameter reduced below 0.1 µm, ***H***). Scale bar: 10 µm (***B–E***).

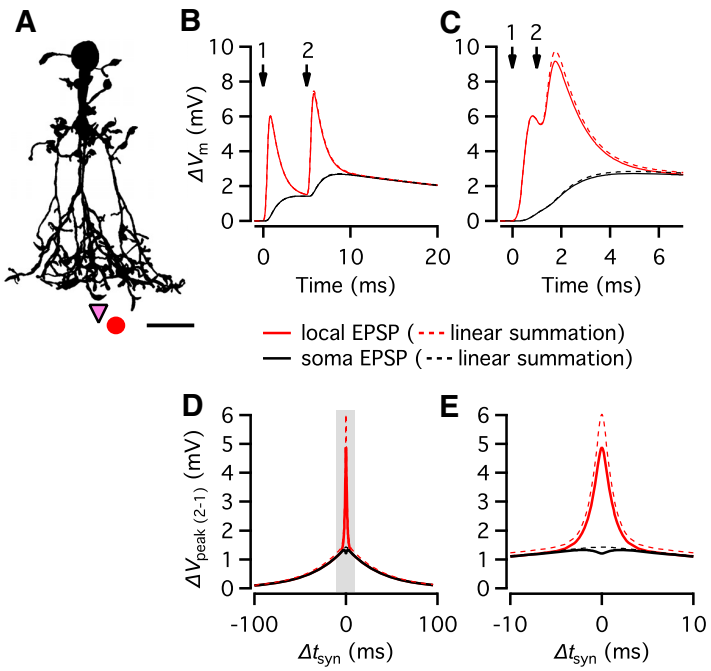

Figure 2. Distinct temporal properties for local versus global EPSP summation in AII amacrines. ***A***, Shape plot of AII. g_{syn} (Fig. 1*A*) injected at distal tip of arboreal dendrite (triangle). Local EPSP recorded at same location (red circle). Scale bar: 10 µm. ***B***, Temporal summation of two EPSPs (Δt_{syn} = 5 ms) evoked by injecting g_{syn}, relative to resting membrane potential (ΔV_m). ***C***, As ***B***, for Δt_{syn} = 1 ms; note increased temporal and sublinear summation. ***D***, Peak amplitude (relative to single response; ΔV_{peak}) as function of Δt_{syn} for local and soma EPSPs. ***E***, As ***D***, expanded for $\Delta t_{syn} = \pm 10$ ms.

local potential closely followed the potential at the soma, both for the single input and during temporal summation in response to higher-frequency input (Fig. 1*B*,*C*). Thus, despite considerable variability of the local EPSP waveforms, synaptic input anywhere in the dendritic tree seems to rapidly (≤5 ms) equilibrate with the rest of the cell and generate a global EPSP, essentially identical to the soma EPSP.

To study the integration of multiple inputs arriving at different dendritic sites, we injected g_{syn} at 15 randomly selected locations and in random order (100 Hz, each synapse activated once per trial; Fig. 1*D*). The EPSP at site 1 was distinctly larger than the soma EPSP when g_{syn} was injected at any of four sites (1–4) in the same arboreal branch (Fig. 1*D*). In contrast, the response at the soma (Fig. 1*D*) was virtually identical to that observed after a 100-Hz stimulus applied at any single location (Fig. 1*B*,*C*). Thus, the enhanced amplitude of a local EPSP spreads over a certain, limited subregion.

Because the morphologic reconstructions and passive membrane parameters are estimated with some uncertainty (Zandt et al., 2018), we examined how local EPSPs are influenced by the passive electrotonic properties R_m (specific membrane resistance) and R_i (cytoplasmic resistivity) and by the dendritic branch diameters. C_m (specific membrane capacitance) was not investigated, as it is not considered to genuinely vary between cells (Hille, 2001). By changing each parameter value and measuring local and soma EPSPs, we investigated the influence on EPSP amplitude and decay kinetics in an AII (Fig. 1*E*).

The modified values of R_m had almost no effect on the peak amplitude of the local EPSP, but had a strong influence on the kinetics of decay, corresponding to altering the membrane time constant of the cell ($\tau = R_m \times C_m$; Fig. 1*F*). Increasing or decreasing R_m by a factor of two changed the rate of decay from the point in time at which the locally injected charge had equilibrated over the cell and the local and global EPSPs were decaying at the same rate. Decreasing R_m by a factor of 10 increased the rate of decay already from the time of the peak of the local EPSP and reduced the peak amplitude of the soma EPSP.

Increasing or decreasing cytoplasmic resistivity (R_i) by a factor of two ($R_i \times 2$, $R_i/2$) strongly increased and decreased the peak amplitude of the local EPSP, respectively, but had almost no influence on the kinetics of the local EPSP or on the amplitude of the soma EPSP (Fig. 1*G*). Increasing or decreasing R_i slightly decreased and increased, respectively, the rate of rise of the soma EPSP. The effect of changing the process diameters (*d*) on the local and soma EPSP was qualitatively very similar to the effect of changing R_i, because of the fact that both properties determine the intracellular resistance between the synaptic location and the rest of the cell. Reduced resistance speeds up the redistribution of charge over the cell membrane. Increasing and decreasing all diameters by 0.1 µm (with no diameter reduced below 0.1 µm) decreased and increased the peak amplitude of the local EPSP by ~30%, respectively (Fig. 1*H*). Changing *d* in this way also moderately (~10%) changed the peak amplitude of the soma EPSP, commensurate with the change in the cell's membrane capacitance when changing *d*. Changing *d* only minimally affected the decay time of the soma EPSP. Taken together, these results suggest that, within realistic limits, the synaptic responses were not influenced by potential errors in the morphologic reconstructions and estimated passive membrane properties (Fig. 1*E*–*H*).

Distinct temporal and spatial properties of local versus global EPSP summation

To further characterize the temporal summation properties, we estimated time windows for local and global synaptic integration by applying g_{syn} twice, separated by an interval Δt_{syn}, at the tip of an arboreal dendrite (Fig. 2*A*,*B*). The first stimulus evoked a local EPSP of ~6 mV and a soma EPSP of ~1.4 mV (Fig. 2*B*). When the second stimulus was applied (Δt_{syn} = 5 ms), most of the charge from the first stimulus had redistributed over the cell and the second EPSPs were both ~1.3 mV larger than the first EPSPs (Fig. 2*B*). This suggested that for temporal intervals ≥5 ms, the summation of local EPSPs will equal the summation of global EPSPs. In contrast, for Δt_{syn} = 1 ms the local membrane potential had not equalized with the rest of the cell when the second stimulus arrived and the local depolarization reached a markedly higher peak amplitude of ~9.2 mV, moderately reduced relative to linear summation (Fig. 2*C*, broken line). This sublinear integration, because of reduced synaptic driving force (cf. Abrahamsson et al., 2012; Vervaeke et al., 2012), reflects that local summation is essentially a nonlinear process (Rall, 1964). In contrast to the markedly larger local EPSP for Δt_{syn} = 1 ms, the global EPSP was practically identical to that observed for Δt_{syn} = 5 ms (~2.7 mV; Fig. 2*B*,*C*).

To systematically investigate the influence of Δt_{syn} on summation, we measured the relative increase (ΔV_{peak}) of local and global EPSPs for $\Delta t_{syn} = \pm 100$ ms (Fig. 2*D*,*E*). For global integration, the time window for summation [full width at half maximum

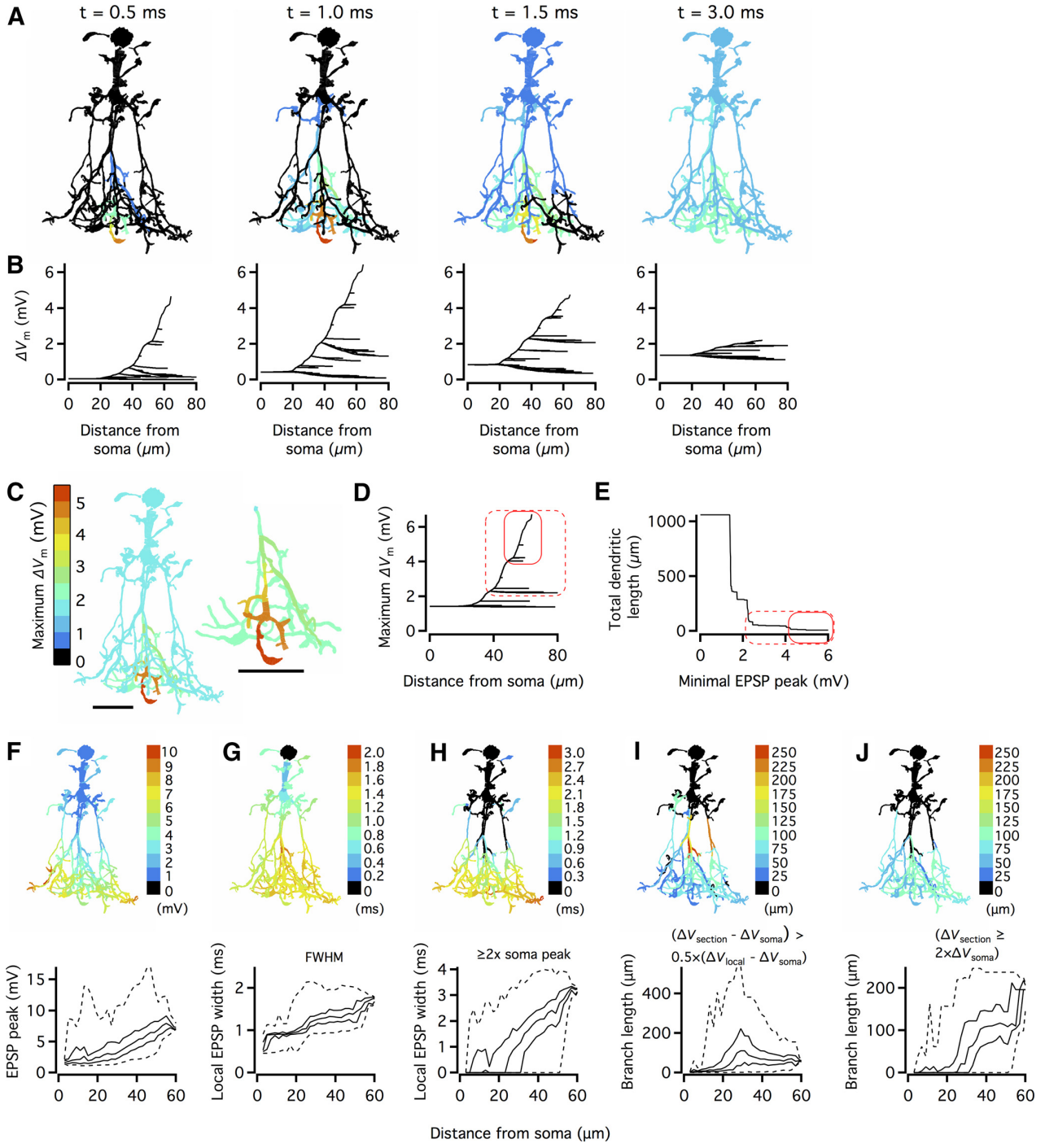

Figure 3. Spatial and temporal characteristics of local EPSPs in All amacrines. ***A***, Color-coded shape plots of ΔV_m as a function of time after injecting g_{syn} at distal arboreal dendrite (orange in leftmost shape plot). Color scale and scaling of shape plots as in ***C***, left. Leak current $E_{rev} = -60$ mV (***A–E***) or $E_{rev} = -50$ mV (***F–J***). ***B***, Space plots of ΔV_m across dendritic tree as function of anatomic distance from soma (neighboring points on dendrites connected by lines) for the same time points as used for shape plots in ***A***. ***C***, Maximum ΔV_m in each compartment during EPSP. Inset, ΔV_m in subtree around synaptic location. Scale bars: 10 μm. ***D***, Maximum ΔV_m in each compartment during EPSP, note that lines for most cell branches overlap. Red lines (***D***, ***E***) mark regions with $\Delta V_m \geq 4$ mV (continuous line) and ≥ 2 mV (dashed line). ***E***, Total dendritic length where ΔV_m reached a minimal EPSP peak amplitude. ***F–J***, Color-coded shape plots (top) for same All as in ***A–E*** and corresponding population data (bottom; $n = 13$ AIIs), with g_{syn} injected sequentially at every branch section. Sholl-like histograms (based on Euclidean distance from soma) display median (Q2), 25% (Q1), and 75% (Q3) percentiles (continuous lines), as well as minimum and maximum (dashed lines), for each bin. ***F***, Peak amplitude of local EPSPs over dendritic tree. ***G***, Width of local EPSPs over dendritic tree; estimated as FWHM of difference between local EPSP and soma EPSP. ***H***, Width of local EPSPs over dendritic tree; estimated as period during which amplitude of local EPSP was $\geq 2\times$ larger than soma EPSP. ***I***, Size of spatial extent of local EPSPs; estimated as total branch length over which depolarization was similar to local EPSP. ***J***, Size of spatial extent of local EPSPs; estimated as total branch length over which depolarization ($\Delta V_{section}$) was $\geq 2\times$ larger than soma EPSP (ΔV_{soma}). See Extended Data Figure 3-1*A–E* for Extended Data.

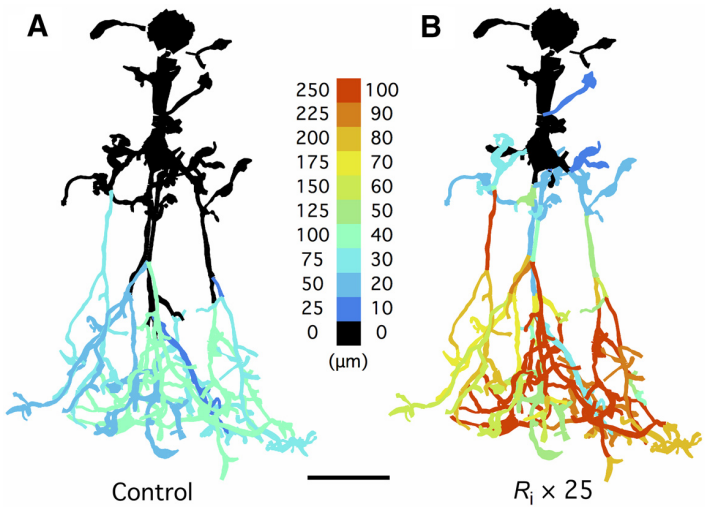

Figure 4. Enhancing dendritic signal attenuation (by increasing the cytoplasmic resistivity; R_i) abolishes clearly identifiable dendritic subunit domains in AII amacrines. ***A***, ***B***, Color-coded shape plots of the spatial extent of the local EPSPs. ***A***, Result for default value of R_i (identical to shape plot in Fig. 3*J*). ***B***, Result obtained after enhancing signal attenuation along dendritic processes by increasing the value of R_i 25-fold. Note how the different regions within previously identifiable subtrees/subunit domains no longer display equal EPSP magnitudes such that the original domains can no longer be clearly identified. Scale bar: 10 μm (***A***, ***B***).

(FWHM)] was ~55 ms (Fig. 2*D*), similar to the cell's membrane time constant (37 ms). A small reduction relative to linear summation could be observed for $\Delta t_{syn} \sim \pm 2$ ms (Fig. 2*E*). The time window for local summation was considerably narrower (FWHM = 3 ms; Fig. 2*E*) and related to the width of the local EPSP (FWHM = 1.8 ms), which in turn is determined by the synaptic conductance waveform and the time for charge redistribution over the membrane. When displayed at higher temporal resolution, sublinear summation could be observed for very short intervals (Fig. 2*E*).

The short time window for local EPSP integration raised the question of the spatial extent over which a local EPSP is larger than the global EPSP. To investigate this, we applied g_{syn} at the distal tip of an arboreal dendrite, recorded the membrane potential at every branch segment as a function of time, and displayed ΔV_m as a function of the cell's morphology (shape plots; Fig. 3*A*) and the anatomic distance from the soma (space plots; Fig. 3*B*) for discrete points in time. During the first ~1 ms, g_{syn} evoked a local depolarization, followed by rapid equilibration and redistribution of charge over the cell during the next 2–3 ms. The maximum depolarization dropped steadily from the synaptic input location (~6 mV) toward the soma, but most regions of the cell reached a maximum of ~1.4 mV, corresponding to the global EPSP, that was nearly constant from the soma to the tips of the unstimulated dendritic processes (Fig. 3*C*,*D*). To measure the spatial extent of depolarization, we calculated the total dendritic length that reached a criterion level of depolarization relative to rest (Fig. 3*E*). Compared with the global depolarization (~1.4 mV), smaller dendritic regions reached increasingly larger depolarizations. Values of ≥4 and ≥2 mV were reached in regions corresponding to ~3% and ~7%, respectively, of the total dendritic length (Fig. 3*D*,*E*).

Properties of local EPSPs obtained for complete sampling over the dendritic tree

The above simulations were limited by the relatively few stimulus locations examined. To investigate the properties of local EPSPs over the entire dendritic tree, we injected g_{syn} sequentially at every branch section (as defined in NEURON) and recorded the membrane potential at all sections. For each of the 13 models (Zandt et al., 2018), we analyzed peak amplitude, duration, and the spatial domain over which the local EPSP spread. As no systematic differences between cells were observed, we summarized the results in Sholl-like histograms based on the Euclidean distance from the soma (Fig. 3*F*–*J*), with color-coded shape plots for one of the cells in Figure 3*F*–*J* and for the other cells in Extended Data Figure 3-1*A*–*E*.

The largest local EPSPs were observed in arboreal dendrites, where the majority of EPSPs reached a peak amplitude ≥5 mV (Fig. 3*F*; Extended Data Fig. 3-1*A*). In lobular dendrites and appendages, the peak amplitudes were considerably lower (1–3 mV), with the largest amplitudes observed in distal dendrites connected via very thin branches. For the population as a whole, the median peak EPSP increased from the soma to the distal arboreal dendrites, with considerable variability as indicated by the maximum amplitudes at the different distances (Fig. 3*F*). The peak amplitude of local EPSPs in arboreal dendrites (>25 μm from the soma) was ~3–8 mV and the peak amplitude in lobular dendrites (<25 μm from the soma) was ~1.5–5 mV.

The duration of the local EPSPs was first calculated from the difference between each local EPSP and the soma EPSP (Fig. 3*G*; Extended Data Fig. 3-1*B*). The FWHM of the local EPSP typically ranged between 0.8 and 1.7 ms and increased with increasing distance from the soma (Fig. 3*G*). When the duration of the local EPSP was instead measured as the period when it was ≥2× larger than the soma EPSP, it varied from 0 to ~3 ms depending on the distance from the soma (Fig. 3*H*; Extended Data Fig. 3-1*C*). In most lobular dendrites, a local EPSP with peak amplitude ≥2× the soma EPSP was not achieved (Fig. 3*H*). In most arboreal dendrites, the amplitude of local EPSPs was ≥2× the soma EPSPs for 1–3 ms (Fig. 3*H*).

The spatial domain of local EPSPs was quantified as the branch length where the peak depolarization ($\Delta V_{section}$; relative to baseline) was similar to the local EPSP [$(\Delta V_{section} - \Delta V_{soma}) > 0.5 \times (\Delta V_{local} - \Delta V_{soma})$; Fig. 3*I*; Extended Data Fig. 3-1*D*]. In lobular dendrites (≤30 μm from the soma), the spatial domain was relatively small (Fig. 3*I*). The largest spatial domain was typically 50–200 μm (~30 μm from the soma) and dropped to ~50–75 μm at the tips of the arboreal dendrites (Fig. 3*I*). This measure shows the branch length where the response amplitude is similar to that at the stimulus site, and hence displays a similar nonlinearity, but does not provide information about the magnitude of the local response or nonlinearity. For comparison, the spatial domain of the local EPSP was also quantified as the total branch length where $\Delta V_{section}$ was ≥2× larger than the soma EPSP (Fig. 3*J*; Extended Data Fig. 3-1*E*). The magnitude of these domains was relatively small in the lobular dendrites (typically 0–10 μm), but in the arboreal dendrites the domains consisted of larger subtrees 50–200 μm in length (Fig. 3*J*). Importantly, this measure shows the dendritic area where a significant local response occurs, and thus where significant nonlinearity of integration will occur.

The shape plots for individual cells clearly indicated that local EPSPs were confined to domains corresponding to specific dendritic subtrees (Fig. 3*J*; Extended Data Fig. 3-1*E*). Within a domain, input at any location evoked a significant depolarization in the entire

subtree. Almost without exception, a local EPSP spread over an entire subtree (observed as differently colored subtrees) for all input locations of that subtree. These domains are likely to correspond to distinct subtrees because the attenuation of signals is relatively small in the centrifugal direction (Zandt et al., 2018). Supporting this interpretation, when attenuation was enhanced by increasing R_i 25-fold, the different regions within previously identifiable subtree domains no longer displayed equal EPSP magnitudes (Fig. 4).

Electrical coupling decreases the time window for global but not local integration

As AII amacrines are electrically coupled by gap junctions, we explored the dynamic impact of increasing junctional conductance (G_j) on local and global EPSPs. We simulated an electrically coupled network of AIIs and injected g_{syn} in the center cell at a lobular (L) or arboreal (A) dendrite (Fig. 5*A*,*B*). For both input locations, increasing G_j (0–2 nS) reduced the amplitude and hastened the decay kinetics of the soma (global) EPSP (Fig. 5*C*,*D*). To verify that this resulted from reduced input resistance and effective membrane time constant (cf. Alcamí and Pereda, 2019), we repeated the simulations after reducing R_m (for an uncoupled cell) and observed that for a ~4-fold reduction, the local and global EPSPs were virtually indistinguishable from those obtained for electrical coupling with G_j = 300 pS (Fig. 5*E*). Note that the similarity between the effects of increasing G_j and reducing R_m only pertains to the behavior of the local and global integration in the stimulated cell, not to the behavior of the network (increasing G_j will cause depolarization of a given cell to depolarize neighboring cells in the network, while a reduction of R_m will not). The strongest reduction of the global EPSP (peak amplitude and width) was seen when the conductance increased from 0 to 500 pS (Fig. 5*F*,*G*). In contrast, increasing G_j had minimal effect on the local EPSP (Fig. 5*C*,*D*), with only minor reduction of peak amplitude and width (Fig. 5*F*,*G*). Similar results were seen for g_{syn} injected at other locations in the dendritic tree. Thus, electrical coupling substantially decreases the time window for global EPSP summation, but remarkably has almost no impact on local EPSP summation.

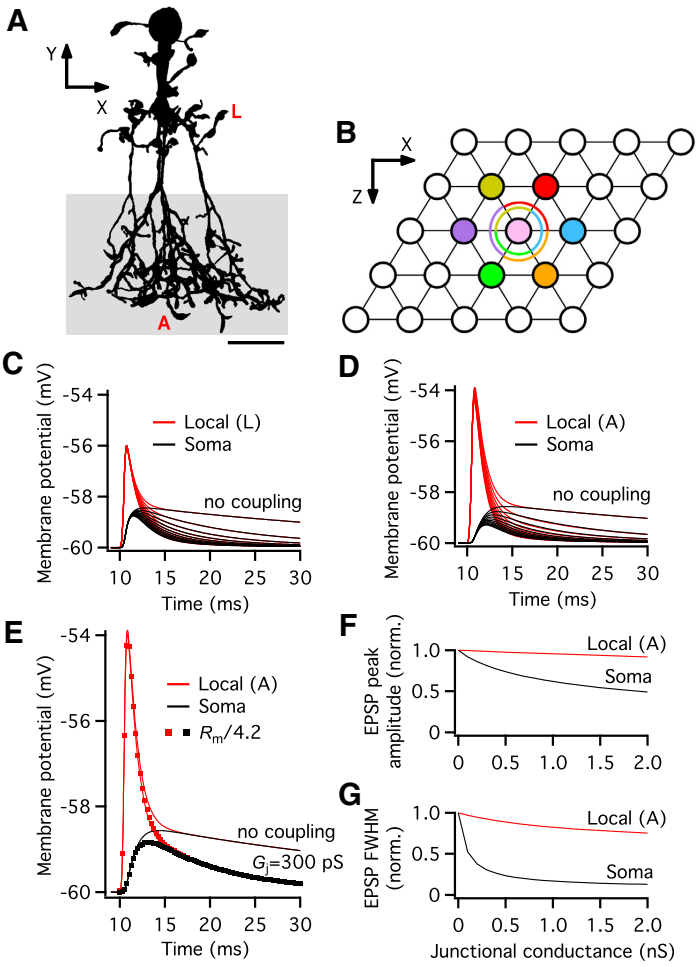

Figure 5. Electrical coupling influences global, but not local integration in AII amacrines. ***A***, Shape plot of AII used for generating electrically coupled network. Shaded area indicates region where electrical synapses could be made with nearest neighbors (strata S5, S4, and proximal part of S3 in the IPL). A (arboreal) and L (lobular) indicate sites for injection of g_{syn} waveform. Scale bar: 10 µm. ***B***, Network of electrically coupled AIIs. Circles indicate cells and black lines indicate pairwise electrical coupling. Sectors within which electrical contacts were made between center cell (pink) and any of its six nearest neighbors indicated by 120° arc of same color as corresponding neighbor (for details, see Hartveit et al., 2019). ***C***, Influence of junctional conductance (G_j; 0–2 nS, steps of 200 pS) on local and soma (global) EPSPs, g_{syn} injected at L. ***D***, As ***C***, g_{syn} injected at A. ***E***, Influence of electrical coupling on local and soma EPSPs was mimicked by reduced specific membrane resistance (R_m), g_{syn} injected at A. For G_j = 300 pS, local and soma EPSPs were similar to EPSPs evoked by g_{syn} without electrical coupling, but with R_m reduced ~4-fold (local EPSP: red squares; soma EPSP: black squares). ***F***, Influence of G_j (ΔG_j = 100 pS) on local and soma EPSP peaks, g_{syn} injected at A. ***G***, Influence of G_j (ΔG_j = 100 pS) on local and soma EPSP widths, g_{syn} injected at A.

Activation of glutamate receptors at arboreal dendrites increases intracellular Ca^{2+} in lobular dendrites

Our simulations predicted that excitatory synaptic input at an arboreal dendrite of an AII amacrine will evoke a large local depolarization and a smaller global depolarization across the entire cell. To measure the local dendritic depolarization experimentally is a considerable challenge because it is difficult to achieve repeated activation of a single, specific rod bipolar synapse required for correlated measurements of the local postsynaptic response, regardless of whether one attempts to measure voltage directly by electrophysiology (Hu et al., 2010; Vervaeke et al., 2012) or imaging (Tran-Van-Minh et al., 2016), or indirectly by Ca^{2+} imaging. Thus, we first examined global integration, specifically asking whether depolarization evoked at an arboreal dendrite can evoke release of glycine at lobular appendages, with concomitant inhibition of OFF-cone bipolar cells (and OFF-ganglion cells). In the first set of experiments, we applied glutamate to distal arboreal dendrites of dye-filled AIIs by ultrafast microiontophoresis and imaged Ca^{2+} in lobular and arboreal dendrites (Fig. 6*A*,*B*). We positioned the tip of the iontophoresis pipette close to a distal arboreal dendrite (Fig. 6*B*,*C*). With the cell in voltage clamp, a brief pulse (1 ms) of glutamate evoked an iontophoretic EPSC (iEPSC) with a fast rise time and slower decay (Fig. 6*D*, top). As a control, we verified that reversing the polarity of the iontophoretic current did not evoke a response (data not shown). In current clamp, the glutamate stimulus evoked an iontophoretic EPSP (iEPSP; peak amplitude ~17 mV; Fig. 6*D*, bottom). With the AII in current clamp, we examined whether

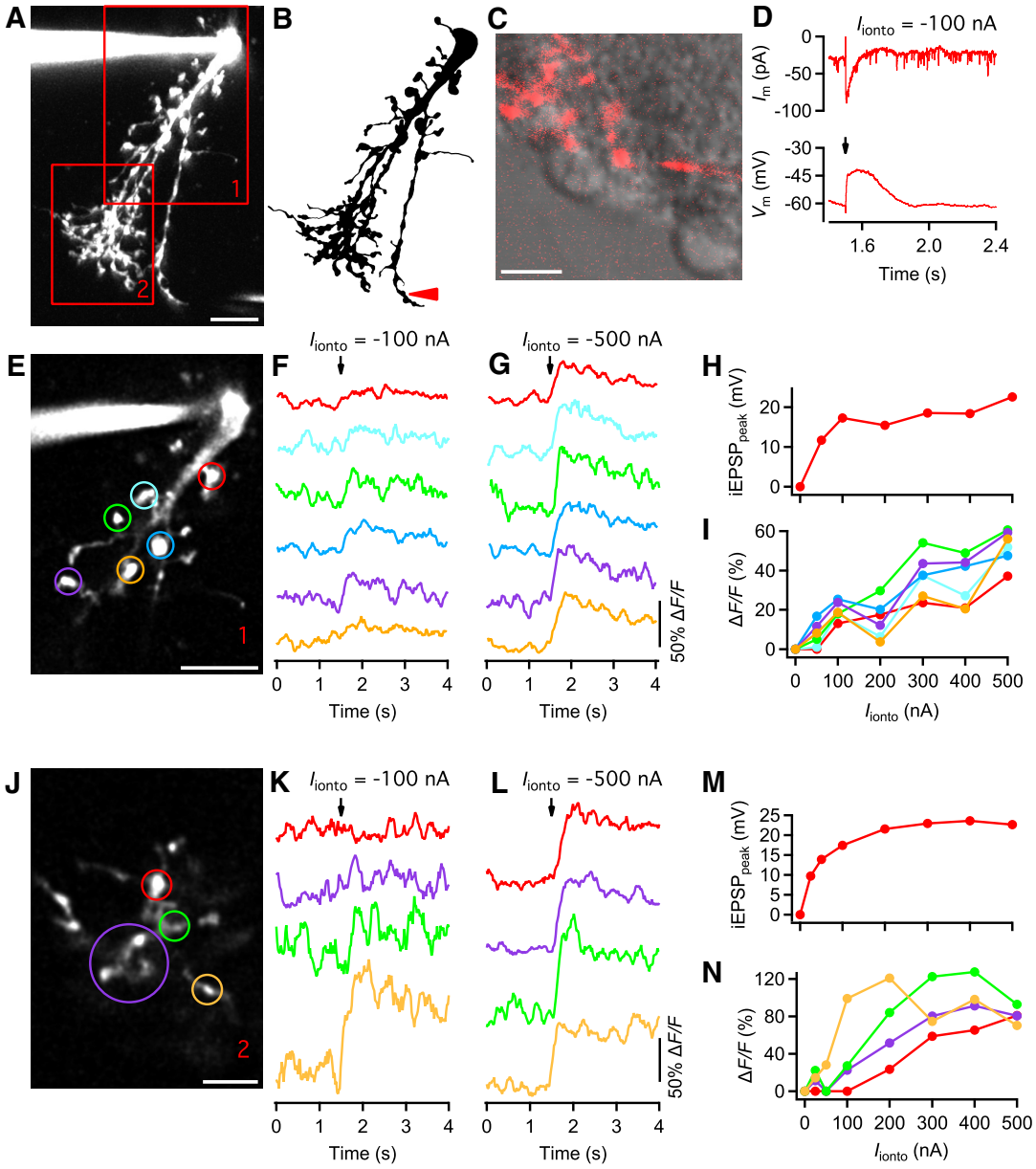

Figure 6. Activation of glutamate receptors at arboreal dendrites increases intracellular Ca^{2+} in lobular dendrites. ***A***, All filled with Alexa 594 and Ca^{2+} indicator (OGB-1) during whole-cell recording. Image stack acquired by MPE microscopy (maximum intensity projection; MIP). Pipette for glutamate microiontophoresis (150 mM; with Alexa 594) partially withdrawn (lower right). Red rectangles indicate subregions displayed separately in ***E*** (1) and ***J*** (2). Scale bar: 10 µm. ***B***, Shape plot of reconstructed AII in ***A***. Arrow head marks position of tip of iontophoresis pipette. ***C***, Fluorescence of arboreal dendrites and iontophoresis pipette (partially withdrawn), overlaid on IR-LSGC image of slice. Scale bar: 10 µm. ***D***, iEPSC (AII in voltage clamp; top) and iEPSP (AII in current clamp; bottom, average of 4) evoked by glutamate pulse (1 ms) applied to arboreal dendrite (***B***, ***C***). Here and later, timing of iontophoretic current stimulus indicated by vertical arrow. For some traces, response onset appears before stimulus onset because of signal smoothing. ***E***, Fluorescence image from single focal plane in subregion 1 of ***A***. Colored circles correspond to ROIs at lobular dendrites for calculating changes in intracellular Ca^{2+} (***F***, ***G***, ***I***). Scale bar: 10 µm. ***F***, Ca^{2+} signals from ROIs in ***E*** evoked by iontophoresis of glutamate (−100 nA, 1 ms, onset at 1.5 s) onto arboreal process as in ***B***, ***C*** with AII in current clamp. Ca^{2+} signal scaling as in ***G***. Here, and in ***G***, ***K***, ***L***, each trace is the average of two repetitions. ***G***, As ***F***, but for larger-amplitude iontophoretic current pulse (−500 nA, 1 ms). ***H***, Peak amplitude of iEPSP as a function of iontophoretic current amplitude (I_{ionto}, 1 ms). Here, and in ***I***, ***M***, ***N*** each point is the average of two repetitions. ***I***, Peak amplitude of Ca^{2+} response ($\Delta F/F$) as a function of I_{ionto}, colors as in ***E***–***G***. ***J***, Fluorescence image from single focal plane in subregion 2 of ***A***. Colored circles correspond to ROIs at arboreal dendrites for calculating changes in intracellular Ca^{2+} (***K***, ***L***, ***N***). Scale bar: 5 µm. ***K***, Ca^{2+} signals from ROIs in ***J*** evoked by iontophoresis of glutamate (−100 nA, 1 ms, onset at 1.5 s) onto arboreal process (***B***, ***C***) with the AII in current clamp. Ca^{2+} signal scaling as in ***L***. ***L***, As ***K***, but for larger-amplitude iontophoretic current pulse (−500 nA, 1 ms). ***M***, Peak amplitude of iEPSP as a function of I_{ionto} amplitude (1 ms). ***N***, Peak amplitude of Ca^{2+} response ($\Delta F/F$) as a function of I_{ionto}, colors as in ***J***–***L***. Intracellular solution: A (K-gluconate).

application of glutamate evoked an increase of Ca^{2+} in lobular dendrites and appendages (Fig. 6*E*). With a low current amplitude (−100 nA), Ca^{2+} transients were evoked in several lobular dendrites, but with relatively small amplitudes and slow rise times (Fig. 6*F*). With a higher current amplitude (−500 nA), Ca^{2+} responses were larger and displayed faster rise times (Fig. 6*G*). For both iEPSPs and Ca^{2+} transients, the amplitude increased in a stimulus-dependent manner (Fig. 6*H*,*I*). For the weakest stimulus tested (−50 nA), some of the lobular dendrites did not display a clear Ca^{2+} increase (Fig. 6*I*). We observed similar stimulus-response relationships when Ca^{2+} responses were measured in arboreal dendrites (Fig. 6*J*–*N*).

Clear increases of Ca^{2+} in lobular dendrites were seen for every AII tested (average $\Delta F/F = 19$, 44, and 47%; 6–9 regions/cell; $n = 3$ cells) with glutamate iontophoresis (−500 nA, 1 ms) to a distal arboreal dendrite (two to four repetitions per cell). These results suggested that when excitatory glutamatergic input to (distal) arboreal dendrites of AIIs generates a sufficiently strong global depolarization, it will evoke a concomitant and proportional increase of Ca^{2+} in lobular dendrites, likely involving activation of voltage-gated Ca^{2+} (Ca_v) channels (Habermann et al., 2003; Balakrishnan et al., 2015; Hartveit et al., 2019).

Global EPSPs mediated by rod bipolar cell input evokes exocytosis in AIIs

We next investigated whether this increase of Ca^{2+} could evoke exocytosis, which can be detected by capacitance measurements (Balakrishnan et al., 2015). Using compartmental modeling, we have demonstrated that a measured capacitance increase must originate in the proximal parts of the dendritic tree, with many, but not all, lobular appendages contributing (Hartveit et al., 2019). To test whether excitatory input at arboreal dendrites can evoke inhibitory output at lobular dendrites, via depolarization-evoked increase of Ca^{2+} and exocytosis of glycine, we performed dual recordings from synaptically connected rod bipolar and AII cells (Fig. 7*A*). After verifying connectivity by the EPSC (~170 pA) evoked in the AII when depolarizing the rod bipolar (Fig. 7*B*), we measured the capacitance of the AII before and after synaptic stimulation, with the AII transiently in current clamp when depolarizing the rod bipolar. The EPSP evoked in the AII (~15 mV) was accompanied by a capacitance increase of ~35 fF (Fig. 7*C*). For a total of five synaptically coupled cell pairs tested in this way, four displayed a capacitance increase (27.2 ± 8.9 fF, range 19–39 fF). We also employed a simpler experiment by first recording an EPSP in a rod bipolar-AII pair and then used the EPSP as a voltage-clamp command to evoke exocytosis in other AIIs (cf. Balakrishnan et al., 2015; Fig. 7*D–H*). For a total of five AIIs, the EPSP command evoked a capacitance increase of 46 ± 25 fF (range

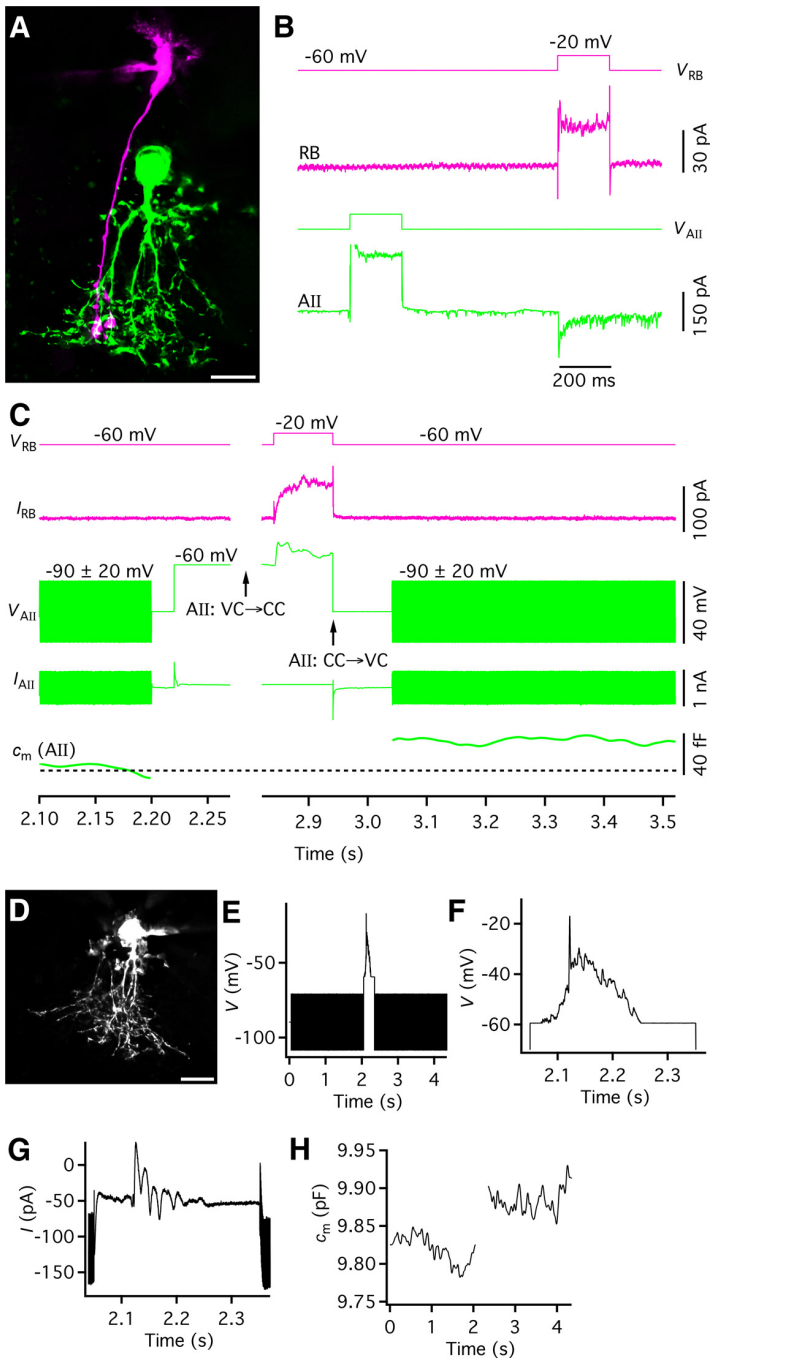

Figure 7. Global EPSP mediated by rod bipolar cell (RB) input evokes exocytosis in AII amacrine. ***A***, Synaptically coupled RB (magenta; Alexa 594) and AII (green; Alexa 488). MIP from wide-field fluorescence image stacks. Same cells in ***A–C***. Scale bar: 10 µm. ***B***, Depolarization (200 ms) of RB (V_{RB}) evoked EPSC in AII. Depolarization (as for RB) of AII (V_{AII}) evoked no response in RB. ***C***, Exocytosis-evoked capacitance increase of AII triggered by EPSP from RB. Magenta traces: RB voltage (V_{RB}) and current (I_{RB}). Green traces: AII voltage (V_{AII}), current (I_{AII}), and capacitance (c_m). During the first period (0–2.2 s), the AII was in voltage clamp and sine wave stimulation (2 kHz) was used to measure baseline capacitance. At 2.2 s, V_{AII} changed to −60 mV. After 50 ms, acquisition temporarily halted and AII switched from voltage to current clamp (AII: VC → CC) to allow bipolar input to evoke EPSP. After resuming acquisition, RB was depolarized (100 ms; onset at ~2.84 s) to evoke EPSP in AII. At end of RB depolarization, AII switched from current to voltage clamp (AII: CC → VC). After 100 ms, capacitance measurement was resumed. Note that AII capacitance increased by ~40 fF after EPSP. ***D***, AII filled with Alexa 594 via patch pipette during whole-cell recording (same cell in ***D–H***). MIP from wide-field fluorescence image stack. Scale bar: 10 µm. ***E***, Sine wave stimulation (2 kHz; ±20 mV from $V_{hold} = -90$ mV) applied before and after AII was depolarized with a voltage-clamp stimulus waveform. Stimulus waveform corresponded to EPSP evoked in a different AII by depolarization of a presynaptic RB. ***F***, Expanded view of voltage-clamp stimulus waveform in ***E***. ***G***, Current evoked in AII by sine wave stimulation and EPSP stimulus waveform (***E***, ***F***). ***H***, Total membrane capacitance (c_m) before and after depolarizing AII with EPSP waveform. The depolarization evoked a capacitance increase of ~50 fF. Intracellular solutions (***A–C***): F (K-gluconate; RB), B (K-gluconate with QX314; AII). Intracellular solution (***D–H***): E (Cs-methanesulfonate).

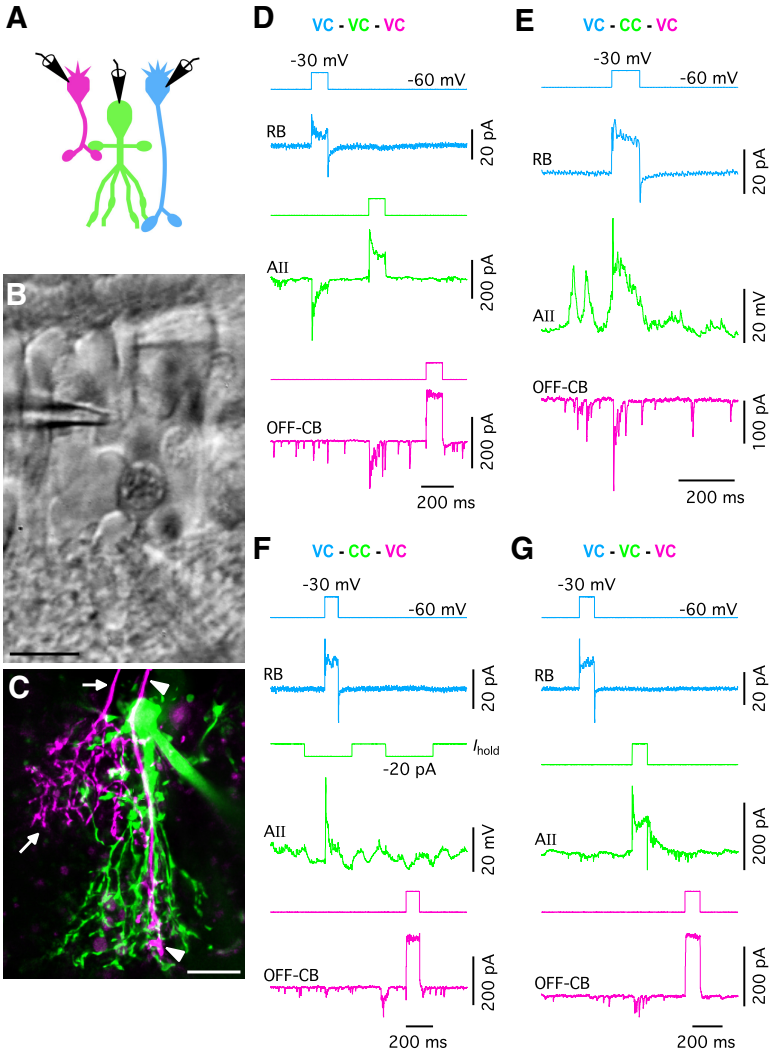

Figure 8. Global integration and input-output coupling via chemical synaptic transmission in AII amacrines. ***A***, Experimental configuration with simultaneous, triple whole-cell voltage-clamp and current-clamp recording (same cells in ***A***–***G***): rod bipolar (RB; blue), AII (green), and type 4 OFF-cone bipolar (OFF-CB; magenta). ***B***, IR-DIC videomicrograph of retinal slice with recording pipettes on RB (top), OFF-CB (middle), and AII (bottom). Scale bar: 10 µm. ***C***, Wide-field fluorescence image (MIP) with RB (magenta; Alexa 594), AII (green; Alexa 488), and OFF-CB (magenta; Alexa 594). Arrowheads indicate axon and axon terminal of RB. Arrows indicate axon and axon terminal of OFF-CB. Scale bar: 10 µm. ***D***, Triple recording of RB, AII, and OFF-CB with all cells in voltage clamp (VC - VC - VC). Depolarization (from −60 to −30 mV, 100 ms) of RB (top blue) evoked inward current in AII, but not in OFF-CB. Same depolarization of AII (top green) evoked inward current in OFF-CB. Same depolarization of OFF-CB (top magenta) evoked no response in RB or AII. Here and in ***E***–***G***, color of trace and recording mode label (VC, CC) corresponds to color of cell in ***A***. ***E***, RB in voltage clamp, AII in current clamp, and OFF-CB in voltage clamp (VC - CC - VC). Depolarization (100 ms) of RB evoked EPSP in AII and inward current in OFF-CB. ***F***, RB in voltage clamp, AII in current clamp, and OFF-CB in voltage clamp (VC - CC - VC). Before and during depolarization (100 ms) of RB, a hyperpolarizing current (−20 pA relative to I_{hold}; top green trace) applied to AII which prevented the EPSP evoked in AII (bottom green trace) from evoking a strong response in the synaptically connected OFF-CB (bottom magenta trace). Here and in ***G***, when OFF-CB was depolarized (100 ms), no response was evoked in the other two cells, consistent with observations in ***D***. ***G***, Following recordings in ***F***, we repeated tests for synaptic connectivity with all three cells in voltage clamp (VC - VC - VC). By the time the depolarizing voltage pulse (100 ms) was applied to RB, exocytosis in this cell had run down and no response was seen in AII. When a depolarizing voltage pulse (100 ms) was applied to AII, an inward current was evoked in OFF-CB, suggesting that the lack of a clear response in OFF-CB when EPSP was evoked during hyperpolarization of AII (***F***) was not caused by rundown of exocytosis in AII. Intracellular solutions: B (K-gluconate with QX314; AII), C (KCl; RB and OFF-CB).

19–87 fF), consistent with the interpretation from the dual recording experiments. Although it is unlikely that the voltage waveform evoked at the lobular dendrites by the voltage command exactly reproduced that occurring at lobular dendrites when the EPSP was originally evoked, the compartmental simulations strongly suggested that an EPSP recorded at the soma is representative of the global EPSP experienced throughout the cell.

Rod bipolar input to an AII evokes synaptic responses in OFF-cone and ON-cone bipolar cells

The increased capacitance of the AII amacrine following excitatory input from the rod bipolar cell, suggested that rod bipolar input to an arboreal dendrite can be transmitted vertically through the AII and evoke glycine release at lobular dendrites, with a response in OFF-cone bipolar and OFF-ganglion cells. To test this directly, we targeted three circuit elements in simultaneous recordings. With an OFF-cone bipolar (type 4), an AII, and a rod bipolar (Fig. 8*A*–*C*) in voltage clamp, we verified the pair-wise synaptic connections. First, depolarizing the rod bipolar evoked an inward current in the AII, but no response in the OFF-cone bipolar (Fig. 8*D*). Second, depolarizing the AII evoked an inward current in the OFF-cone bipolar (which was recorded with high intracellular chloride concentration), but (as expected) no response in the rod bipolar (Fig. 8*D*). Finally, depolarizing the OFF-cone bipolar did not evoke a response in either the AII or the rod bipolar (Fig. 8*D*). We then changed the recording configuration of the AII to current clamp, to examine whether synaptic input from the rod bipolar could be efficiently transmitted through the AII and evoke transmitter release at the lobular appendages (Fig. 8*E*). Depolarizing the rod bipolar evoked an EPSP in the AII and a synchronous inward current in the OFF-cone bipolar (Fig. 8*E*). This verified the presence of vertical transmission through the AII and also suggested that with the AII in voltage clamp (Fig. 8*D*), input from the rod bipolar was unable to depolarize the lobular dendrites and evoke a response in the OFF-cone bipolar. The lack of response in the OFF-cone bipolar with the AII in voltage clamp also suggested that there was no direct synaptic connection between the rod bipolar and OFF-cone bipolar, and no pathways that bypassed the AII. To support this interpretation, we repeated the experiment with the AII in current clamp, but with the cell hyperpolarized by negative current injection. In this condition, the EPSP evoked in the AII (by the depolarization of the rod bipolar) was insufficient to evoke a response in the OFF-cone bipolar (Fig. 8*F*,*G*). These results provide direct evidence that rod bipolar input can be transmitted "vertically" through an AII and evoke exocytosis at the lobular dendrites.

In a second triple recording, we encountered another configuration with three synaptically connected cells: a rod bipolar connected to an AII which was connected via an electrical synapse to an ON-cone bipolar cell (type 6; Fig. 9*A*–*C*). With all cells in voltage clamp, we verified the pair-wise synaptic connections (Fig. 9*D*,*E*). First, depolarizing (but not hyperpolarizing) the rod bipolar evoked a (small) inward current in the AII, but no response in the ON-cone bipolar (Fig. 9*D*,*E*). Second, hyperpolarizing (Fig. 9*D*) and depolarizing (Fig. 9*E*) the AII or the ON-cone bipolar evoked outward and inward currents, respectively, in the other (nonstepped) cell, but no response in the rod bipolar (Fig. 9*D*,*E*). When we changed the AII to the current-clamp configuration, depolarization of the rod bipolar evoked an EPSP in the AII and a synchronous inward current in the ON-cone bipolar (Fig. 9*F*). This suggested that with the AII in voltage clamp (Fig. 9*E*), input from the rod bipolar was prevented from depolarizing the arboreal dendrites sufficiently to evoke a current response in the ON-cone bipolar. In contrast, with the AII in current clamp, the EPSP evoked by rod bipolar input generated an inward current in the ON-cone bipolar, consistent with the response evoked by depolarizing the AII in voltage clamp. We also repeated the experiment with the AII in current clamp, but with its membrane potential hyperpolarized by negative current injection. In this condition, the EPSP evoked in the AII (by the depolarization of the rod bipolar) was still able to evoke an inward current in the ON-cone bipolar, overlayed on an outward current evoked by the hyperpolarization of the AII (Fig. 9*G*). These results provide direct evidence that rod bipolar synaptic input can be transmitted through the arboreal tree of an AII and evoke a response in ON-cone bipolar cells electrically coupled to the AII.

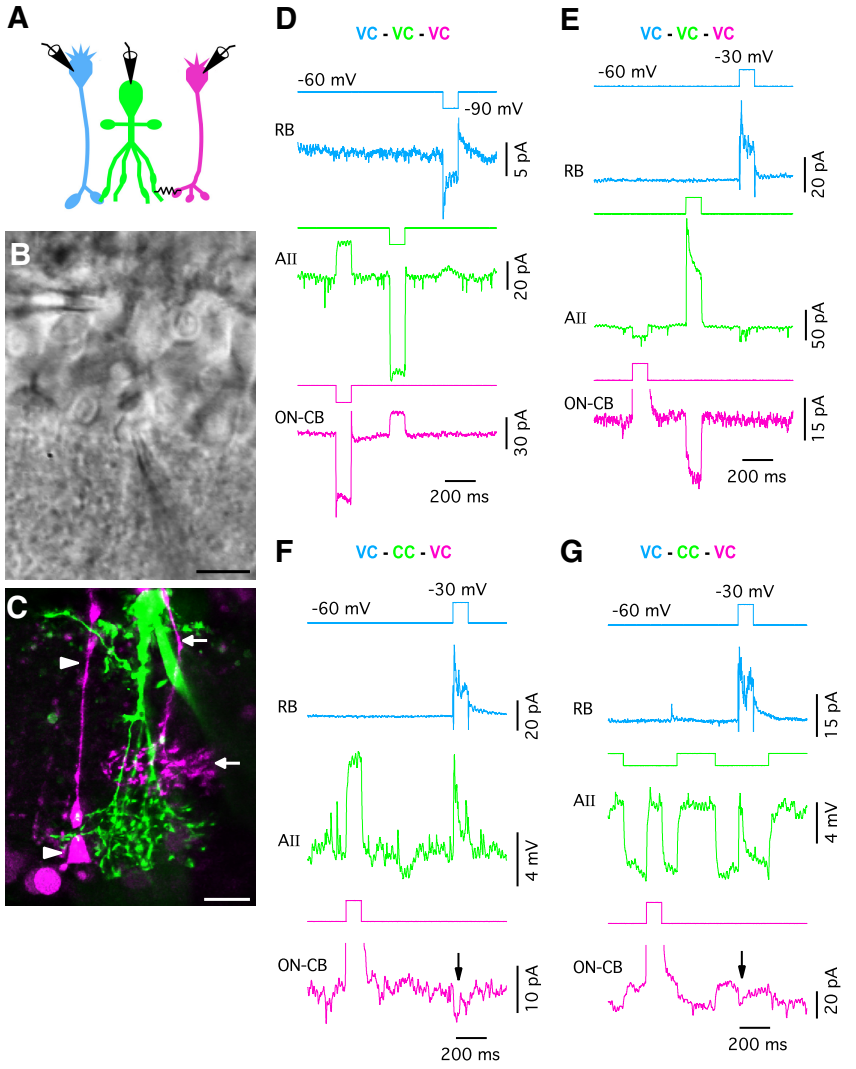

Figure 9. Global integration and input-output coupling via combined chemical and electrical synaptic transmission in AII amacrines. ***A***, Experimental configuration with simultaneous, triple whole-cell voltage-clamp and current-clamp recording (same cells in ***A***–***G***): rod bipolar (RB; blue), AII (green) and type 6 ON-cone bipolar (ON-CB; magenta). ***B***, IR-DIC videomicrograph of retinal slice with recording pipettes on RB (top), ON-CB (middle right, not in focus), and AII (bottom). Scale bar: 10 μm. ***C***, Wide-field fluorescence image (MIP) with RB (magenta; Alexa 594), AII (green; Alexa 488), and ON-CB (magenta; Alexa 594). Arrowheads indicate axon and axon terminal of RB. Arrows indicate axon and axon terminal of ON-CB. Scale bar: 10 μm. ***D***, Triple recording of RB, AII, and ON-CB with all cells in voltage clamp (VC - VC - VC). Hyperpolarization (from −60 to −90 mV, 100 ms) of RB (top blue) evoked no response in AII or ON-CB. Same hyperpolarization of AII (top green) evoked outward current in ON-CB. Same hyperpolarization of ON-CB (top magenta) evoked outward current in AII. Here and in ***E***–***G***, color of trace and recording mode label (VC, CC) corresponds to color of cell in ***A***. ***E***, As in ***D***, but with depolarizing voltage pulses. Depolarization (from −60 to −30 mV, 100 ms) of RB (top blue) evoked inward current in AII, but no response in ON-CB. Same depolarization of AII (top green) evoked inward current in ON-CB. Same depolarization of ON-CB (top magenta) evoked inward current in AII. Outward current evoked by depolarization of ON-CB has been truncated. ***F***, RB in voltage clamp, AII in current clamp, and ON-CB in voltage clamp (VC - CC - VC). Depolarization (100 ms) of RB evoked EPSP in AII and inward current in ON-CB (arrow). Same depolarization of ON-CB evoked depolarization (electrical PSP) in AII. ***G***, RB in voltage clamp, AII in current clamp, and ON-CB in voltage clamp (VC - CC - VC). When RB or ON-CB was depolarized (100 ms), hyperpolarizing current pulses (−20 pA relative to I_{hold}; top green trace) were applied to the AII. Hyperpolarization of AII did not prevent RB-evoked EPSP (bottom green trace) from evoking an inward current (arrow) in electrically connected ON-CB (bottom magenta trace). When ON-CB was depolarized (100 ms), a depolarization (electrical PSP) was evoked in AII. Intracellular solutions: B (K-gluconate with QX314; AII and RB), C (KCl; ON-CB).

Signal transmission between ON-cone bipolar cells connected to a common AII amacrine via electrical synapses

When targeting AII and bipolar cells for triple recordings, we also encountered the configuration with an AII connected via electrical synapses to two ON-cone bipolars (type 6 and type 8; Fig. 10*A*–*C*). With all cells in voltage clamp, we depolarized and hyperpolarized each cell sequentially (Fig. 10*D*). A voltage pulse in either of the ON-cone bipolars evoked a response in the AII and a voltage pulse in the AII evoked a response in both ON-cone bipolars. With the AII in current clamp, a voltage pulse in either ON-cone bipolar evoked not only a depolarization (or hyperpolarization) of the AII, but a concomitant response in the other ON-cone

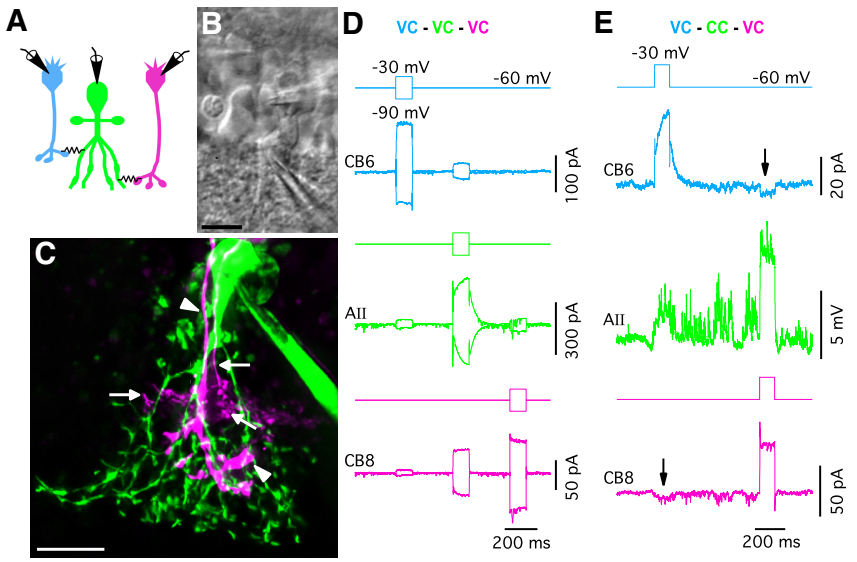

Figure 10. Global integration and input-output coupling via electrical synaptic transmission in AII amacrines. ***A***, Schematic figure of experimental configuration with simultaneous, triple whole-cell voltage-clamp and current-clamp recording (same cells in ***A–E***): type 6 ON-cone bipolar (CB6; blue), AII (green), and type 8 ON-cone bipolar (CB8; magenta) connected by electrical synapses. ***B***, IR-DIC videomicrograph of retinal slice with recording pipettes on CB8 (top), CB6 (middle), and AII (bottom). Scale bar: 10 µm. ***C***, Wide-field fluorescence image (MIP) with CB8 (magenta; Alexa 594), AII (green; Alexa 488), and CB6 (magenta; Alexa 594). Arrowheads indicate axon and axon terminal of CB8. Arrows indicate axon and axon terminal of CB6. Scale bar: 10 µm. ***D***, Triple recording of CB6, AII, and CB8 with all cells in voltage clamp (VC - VC - VC). Hyperpolarization/depolarization of CB6/AII evoked inward/outward current in same cell and outward/inward currents in AII and CB8/CB6 and CB8. Hyperpolarization/depolarization of CB8 evoked inward/outward current in same cell and outward/inward currents in AII, but no response in CB6. ***E***, As ***D***, but with AII in current clamp (VC - CC - VC); only responses evoked by depolarizations have been illustrated. Depolarization of CB6/CB8 evoked depolarization of AII and inward current in CB8 (arrow)/CB6 (arrow). Intracellular solutions: B (K-gluconate with QX314; AII), C (KCl; CB6), D (K-gluconate; CB8).

bipolar (illustrated for depolarizing voltage pulses in Fig. 10*E*). This further supported the conclusion that the arboreal dendritic tree of an AII amacrine mediates transfer of signals between cells connected via electrical synapses with the AII.

NMDA receptors (NMDARs) contribute to depolarization-evoked Ca^{2+} responses in AII dendrites

The vertical signal transmission that links inputs and outputs at arboreal and lobular dendrites in an AII, is mediated by global integration. This raises the question of a functional role for the larger-amplitude, transient local dendritic responses which integrate over smaller subregions of the dendritic tree. Ca_v channels and NMDARs are strong candidates for responding to and potentially amplifying local depolarizations (Higley and Sabatini, 2012). There is evidence for Ca_v channels at lobular dendrites (Habermann et al., 2003; Balakrishnan et al., 2015; Hartveit et al., 2019) and recent work from our laboratory demonstrated Ca^{2+}-permeable NMDARs extrasynaptically at arboreal and lobular dendrites (Veruki et al., 2019; see also Kothmann et al., 2012). With glutamate bound to these receptors, depolarization should relieve the Mg^{2+}-dependent channel block and allow them to function as a voltage-gated Ca^{2+} source.

With Ca^{2+} imaging at multiple locations during whole-cell recording of an AII (Fig. 11*A*), we observed depolarization-evoked Ca^{2+} responses in both lobular and arboreal dendrites (Fig. 11*B*,*C*). Partial suppression by the antagonist CPP suggested that NMDARs contributed to the Ca^{2+} responses in both lobular and arboreal dendrites (Fig. 11*C*). When all regions with Ca^{2+} responses were analyzed together, the maximum suppression evoked by CPP was 52%, with Ca^{2+} responses recovering after washout of CPP (Fig. 11*D*). For a total of four AII amacrines, the average suppression was 44 ± 17% (range 22–60%; $p = 0.01363$, paired t test). The depolarization-evoked increase of intracellular Ca^{2+} in the presence of CPP is likely to be mediated by Ca_v channels. Ca^{2+} responses were observed in both lobular and arboreal dendrites and were partially blocked by CPP, suggesting that Ca_v channels and NMDARs are present in both locations (cf. Grimes et al., 2021). The block evoked by CPP suggests that sufficient glutamate is bound to the NMDARs (cf. Veruki et al., 2006, 2019) to allow depolarization to trigger channel gating. This could be of particular importance for local responses that integrate over dendritic subregions. Whereas it cannot be excluded that depolarization-evoked increase of Ca^{2+} in arboreal dendrites could, at least partially, be mediated by Ca^{2+} influx in axon terminals of gap junction-coupled ON-cone bipolar cells, the measured increase must have occurred in the AII, as we did not observe dye coupling for the Ca^{2+} indicator (OGB-1).

Discussion

The assumption of electrotonic compactness of the AII (Vardi and Smith, 1996; Cembrowski et al., 2012; Diamond, 2017), based on cell size, was challenged by recent work from our laboratory which demonstrated clear frequency-dependent electrotonic filtering (Zandt et al., 2018). Here, we used morphologically realistic, conductance-based modeling to develop a series of predictions that were tested experimentally. Our results suggest that the cellular morphology and electrotonic properties of the AII enable simultaneous local and global integration in response to excitatory input at different locations of the dendritic tree. Importantly, whereas the amplitude of local EPSPs depends on location in the dendritic tree and is resistant to electrical coupling, the amplitude and time course of global EPSPs are essentially independent of synaptic input location and markedly reduced by electrical coupling.

Simultaneous local and global integration in AIIs

Global integration occurs when the AII as a whole integrates synaptic input, and the voltage in the entire dendritic tree follows the membrane potential measured at the soma. The time window for global integration, with summation of non-neighboring inputs, is determined by the membrane time constant (Koch et al., 1996) and therefore independent of the exact morphology of the AII. This longer time window corresponds functionally to the AII operating as an integrator of synaptic activity.

For the AII, local integration occurs when excitatory input at a dendrite evokes a larger depolarization than in the rest of the cell. Local EPSPs correspond to strong charging of the membrane and are characterized by fast rise times and double-exponential decays. The enhanced local depolarization (predicted by local input impedance: Zandt et al., 2018; see also Schmidt-

Hieber et al., 2007; Nörenberg et al., 2010) follows the time course of the synaptic conductance. The initial rapid decay corresponds to fast charge redistribution and equilibration of the voltage differences between the different subcellular compartments (Rall, 1964) and the late decay follows the decay of the global EPSP. The initial, fast equilibration imparts a fast "local" membrane time constant and enables dendritic signal processing with high temporal precision (coincidence detection; Williams and Stuart, 2002; Schmidt-Hieber et al., 2007). It will be technically demanding to investigate local integration experimentally, but combining two-photon uncaging and voltage imaging might enable both generation and measurement of local EPSPs.

Sublinear and supralinear integration in AII dendritic processes

With a passive AII, we observed distance-dependent sublinear integration, with a temporal window equal to that for local integration. Supralinear integration (with EPSPs larger than predicted from linear summation; Tran-Van-Minh et al., 2016) may be mediated by activation of Ca_v channels or NMDARs, both of which are found at lobular appendages (Habermann et al., 2003; Balakrishnan et al., 2015; Hartveit et al., 2019; Veruki et al., 2019). For arboreal dendrites there is evidence for extrasynaptic NMDARs (Veruki et al., 2019) and our results suggest that these processes also express Ca_v channels (cf. Grimes et al., 2021). As NMDARs are involved in plasticity of the Cx36-dependent gap junctions between AIIs (Kothmann et al., 2012), depolarization by coincident synaptic inputs could be a mechanism for spatially restricted control of plasticity (cf. Losonczy et al., 2008). Immunolabeling for phosphorylated Cx36 demonstrated significant heterogeneity across the arboreal dendrites (Kothmann et al., 2012), suggesting prominent local control. Activation of dendritic NMDARs could also extend the brief time window of summation of excitatory inputs (Polsky et al., 2004).

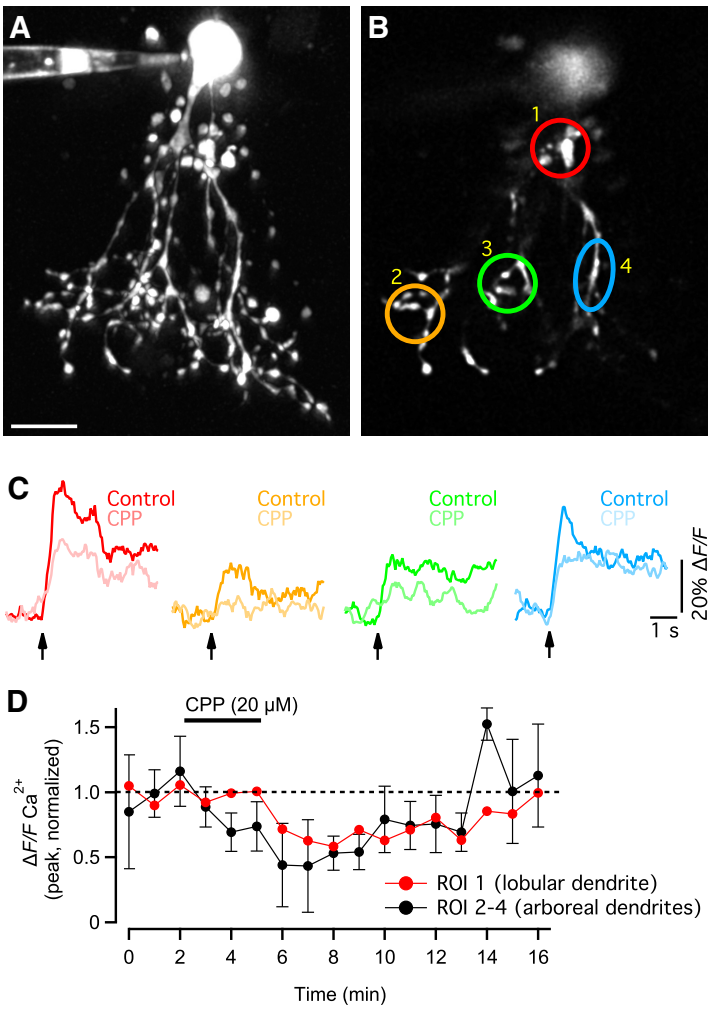

Figure 11. NMDARs contribute to depolarization-evoked Ca^{2+} responses in AII dendrites. ***A***, AII filled with Alexa 594 and OGB-1 (same cell in ***A–D***). MIP generated from MPE fluorescence stack at end of recording, beading of processes caused by repeated depolarization. Scale bar: 10 μm (***A***, ***B***). ***B***, Single focal plane of image stack in ***A***. Colored circles indicate ROIs in lobular (ROI 1) and arboreal (ROIs 2–4) dendrites for measuring intracellular Ca^{2+} (***C***, ***D***). ***C***, Ca^{2+} signals from ROIs in ***B*** evoked by depolarization (100 ms, −60 to 0 mV; onset indicated by arrows), in the control condition (saturated colors) and in the presence of CPP to block NMDARs (pale colors). In both conditions, bath solution contained drugs to block voltage-gated Na^+ channels and $GABA_A$, glycine and non-NMDA receptors. Traces for ROI 2, 3, and 4 are averages of two, two, and three repetitions, respectively. ***D***, Peak amplitude of Ca^{2+} responses in lobular (ROI 1) and arboreal (ROIs 2–4; mean ± SD) dendrites evoked by depolarization (as in ***C***; 60-s intervals) as function of time. Measurements normalized to average of first three data points in control. Time 0 (first measurement) was 22 min after establishing the whole-cell configuration. Period when CPP was added to the bath solution is indicated by the horizontal bar. Intracellular solution: A (K-gluconate).

Simulations suggested local summation for synaptic inputs arriving within a time window of ~1.1 ms and within a region of ~5% of the total branch length of an AII. With a maximum release rate from a rod bipolar of 2–3 kHz per release site (Oltedal and Hartveit, 2010), local summation would allow integration of two to three quantal responses. Within this temporal and spatial region, integration is moderately sublinear, with the summed EPSP reduced ~10% compared with linear summation. With input from additional release sites, the extent of sublinear integration could increase further. For cerebellar stellate cell interneurons, Vervaeke et al. (2012) found that common synaptic input and electrical coupling could compensate for sublinear summation. As neighboring, electrically coupled AIIs can receive common bipolar input, it will be interesting to test whether a similar mechanism is relevant here.

Electrical coupling impacts global but not local synaptic integration in AIIs

The strength of coupling between AIIs is considered to be important for noise reduction (Smith and Vardi, 1995) and will impact the cells' spatial receptive field properties. Our results suggest that the strength of coupling, influenced by ambient light intensity (O'Brien and Bloomfield, 2018), will also have a marked effect on the signal integration of AIIs, as enhanced junctional conductance reduces the duration (and amplitude) of the global EPSP, thereby reducing the efficiency of temporal summation. Remarkably, however, the strength of electrical coupling only

minimally influenced local EPSPs. If local EPSPs in the arboreal dendrites (where most gap junctions are located) are important for activating NMDARs involved in plasticity of coupling, our results predict that the conditions for activating the intracellular signaling pathways are not themselves influenced by the strength of coupling. Further work is required to test this experimentally.

Direct evidence for vertical synaptic integration and multifunctional microcircuits of AIIs

Rod bipolars provide glutamatergic input at arboreal dendrites (Ghosh et al., 2001; Li et al., 2002; Hartveit et al., 2018) which also are the site of electrical synapses with other AIIs and axon terminals of ON-cone bipolars (Strettoi et al., 1992, 1994; Veruki and Hartveit, 2002a, b). OFF-cone bipolars provide glutamatergic input at lobular dendrites (Strettoi, 1992, 1994; Veruki et al., 2003; Graydon et al., 2018) and OFF responses (in addition to ON responses) have been detected in AIIs under light-adapted conditions (Xin and Bloomfield, 1999; Pang et al., 2007). In addition, AIIs inhibit OFF-cone bipolars at glycinergic synapses made by lobular appendages (Pourcho and Goebel, 1985; Strettoi et al., 1992, 1994; Graydon et al., 2018; Hartveit et al., 2019). This polarized dendritic morphology with segregated inputs and outputs has raised the question whether an AII primarily operates as multiple, independent microcircuits or whether there is also a strong element of global integration with crossover inhibition (arboreal → lobular; Werblin, 2010) and crossover excitation (lobular → arboreal). Whereas arboreal → lobular transmission is proposed to mediate signal transfer in scotopic vision (for review, see Bloomfield and Dacheux, 2001; see also Murphy and Rieke, 2008) and crossover inhibition during photopic vision (Manookin et al., 2008; Münch et al., 2009), the frequency-dependent attenuation is actually lower for transmission in the lobular → arboreal direction (Zandt et al., 2018). Despite considerable support for such vertical signal transmission in the AII, it is based on indirect evidence. When interrogating circuit mechanisms to reveal signal flow through retinal networks, there is a risk when experimental results are interpreted based on a small number of canonical circuits and the ability of pharmacological tools to precisely dissect the contributions of specific synapses (cf. Sharpe and Stockman, 1999). This is particularly relevant for the AII which is connected to a large number of different neurons (Marc et al., 2014). Thus, when using visual stimulation, it cannot be known a priori that any scotopic visual response in an AII originates from rod bipolar input to the arboreal dendrites.

The efficiency of vertical signal transmission in AIIs is likely to be influenced by active conductances (Tian et al., 2010; Cembrowski et al., 2012). Although voltage-gated Na^+ channels could be an important amplification mechanism, they cannot be a requirement for vertical transmission, as their contribution was eliminated in our experiments. Near visual threshold the rod bipolar inputs to an AII may be too weak to evoke measurable output by exocytosis at the lobular dendrites, despite the negative activation threshold of the Ca_v channels (−55 mV; Habermann et al., 2003). Instead, larger-amplitude local EPSPs in the distal arboreal dendrites could evoke output directly onto ganglion cell somata, suggested by recent evidence for chemical synaptic contacts made by arboreal dendrites (Grimes et al., 2021). This could explain that in mouse, rod-driven signals near visual threshold can be measured in some OFF-ganglion cells, but not in OFF-cone bipolars (Arman and Sampath, 2012).

Dendritic subunits as a general feature of amacrine cells

The dendritic subunits in AIIs are reminiscent of those in the larger dendritic trees of A17 and starburst amacrines and retinal ganglion cells (Koch et al., 1982; Grimes et al., 2009, 2010; Poleg-Polsky et al., 2018; Ran et al., 2020). AIIs receive synaptic input from other amacrine cells, with evidence for both glycinergic and GABAergic inhibition (Gill et al., 2006; Weiss et al., 2008; Park et al., 2020). Depending on the timing of presynaptic release relative to visual stimuli, the kinetics of the postsynaptic receptors, and the subcellular location of the inhibitory synapses, inhibitory input could play a dynamic role in compartmentalizing dendritic signaling and reducing global integration (Chen et al., 2017; Poleg-Polsky et al., 2018; see also Mel et al., 2017). Dynamic inhibitory control of dendritic subunits is likely to be of general importance for amacrine cells, including cells with small dendritic trees, as well as for inhibitory interneurons in other regions of the CNS.

References

Abrahamsson T, Cathala L, Matsui K, Shigemoto R, DiGregorio DA (2012) Thin dendrites of cerebellar interneurons confer sublinear synaptic integration and a gradient of short-term plasticity. Neuron 73:1159–1172.

Alcamí P, Pereda AE (2019) Beyond plasticity: the dynamic impact of electrical synapses on neural circuits. Nat Rev Neurosci 20:253–271.

Arman AC, Sampath AP (2012) Dark-adapted response threshold of OFF ganglion cells is not set by OFF bipolar cells in the mouse retina. J Neurophysiol 107:2649–2659.

Balakrishnan V, Puthussery T, Kim M-H, Taylor WR, von Gersdorff H (2015) Synaptic vesicle exocytosis at the dendritic lobules of an inhibitory interneuron in the mammalian retina. Neuron 87:563–575.

Bloomfield SA, Dacheux RF (2001) Rod vision: pathways and processing in the mammalian retina. Prog Ret Eye Res 20:351–384.

Branco T, Häusser M (2010) The single dendritic branch as a fundamental functional unit in the nervous system. Curr Opin Neurobiol 20:494–502.

Carnevale NT, Hines ML (2006) The NEURON book. Cambridge: Cambridge University Press.

Castilho Á, Ambrósio AF, Hartveit E, Veruki ML (2015) Disruption of a neural microcircuit in the rod pathway of the mammalian retina by diabetes mellitus. J Neurosci 35:5422–5433.

Cembrowski MS, Logan SM, Tian M, Jia L, Li W, Kath WL, Riecke H, Singer JH (2012) The mechanisms of repetitive spike generation in an axonless retinal interneuron. Cell Rep 1:155–166.

Chen M, Lee S, Zhou ZJ (2017) Local synaptic integration enables ON-OFF asymmetric and layer-specific visual information processing in vGluT3 amacrine cell dendrites. Proc Natl Acad Sci USA 114:11518–11523.

Chun MH, Han SH, Chung JW, Wässle H (1993) Electron microscopic analysis of the rod pathway of the rat retina. J Comp Neurol 332:421–432.

Diamond JS (2017) Inhibitory interneurons in the retina: types, circuitry, and function. Annu Rev Vis Sci 3:1–24.

Dodt H-U, Frick A, Kampe K, Zieglgänsberger W (1998) NMDA and AMPA receptors on neocortical neurons are differentially distributed. Eur J Neurosci 10:3351–3357.

Euler T, Detwiler PB, Denk W (2002) Directionally selective calcium signals in dendrites of starburst amacrine cells. Nature 418:845–852.

Fain G (1981) Integration by spikeless neurones in the retina. In: Neurones without impulses (Roberts A, Bush BMH, eds), pp 29–59. Cambridge: Cambridge University Press.

Fernández-Alfonso T, Nadella KMNS, Iacaruso MF, Pichler B, Roš H, Kirkby PA, Silver RA (2014) Monitoring synaptic and neuronal activity in 3D with synthetic and genetic indicators using a compact acousto-optic lens two-photon microscope. J Neurosci Methods 222:69–81.

Ghosh KK, Haverkamp S, Wässle H (2001) Glutamate receptors in the rod pathway of the mammalian retina. J Neurosci 21:8636–8647.

Gill SB, Veruki ML, Hartveit E (2006) Functional properties of spontaneous IPSCs and glycine receptors in rod amacrine (AII) cell in the rat retina. J Physiol 575:739–759.

Gillis KD (1995) Techniques for membrane capacitance mesurements. In: Single-channel recording, Ed 2 (Sakmann B, Neher E, eds), pp 155–198. New York; London: Plenum.

Graydon CW, Lieberman EE, Rho N, Briggman KL, Singer JH, Diamond JS (2018) Synaptic transfer between rod and cone pathways mediated by AII amacrine cells in the mouse retina. Curr Biol 28:2739–2751.

Grimes WN, Li W, Chávez AE, Diamond JS (2009) BK channels modulate pre- and postsynaptic signaling at reciprocal synapses in retina. Nat Neurosci 12:585–592.

Grimes WN, Zhang J, Graydon CW, Kachar B, Diamond JS (2010) Retinal parallel processors: more than 100 independent microcircuits operate within a single interneuron. Neuron 65:873–885.

Grimes WN, Sedlacek M, Musgrove M, Nath A, Tian H, Hoon M, Rieke F, Singer JH, Diamond JS (2021) Dendro-somatic synaptic inputs to ganglion cells contradict receptive field and connectivity conventions in the mammalian retina. Curr Biol. Available at https://doi.org/10.1016/j.cub.2021.11.005.

Habermann CJ, O'Brien BJ, Wässle H, Protti DA (2003) AII amacrine cells express L-type calcium channels at their output synapses. J Neurosci 23:6904–6913.

Hartveit E, Veruki ML (2019) Combining multiphoton excitation microscopy with fast microiontophoresis to investigate neuronal signaling. In: Multiphoton microscopy (Hartveit E, ed), pp 131–159. New York: Humana Press/Springer Nature.

Hartveit E, Zandt BJ, Madsen E, Castilho Á, Mørkve SH, Veruki ML (2018) AMPA receptors at ribbon synapses in the mammalian retina: kinetic models and molecular identity. Brain Struct Funct 223:769–804.

Hartveit E, Veruki ML, Zandt BJ (2019) Capacitance measurement of dendritic exocytosis in an electrically coupled inhibitory retinal interneuron: an experimental and computational study. Physiol Rep 7:e14186.

Helmstaedter M, Briggman KL, Turaga SC, Jain V, Seung HS, Denk W (2013) Connectomic reconstruction of the inner plexiform layer in the mouse retina. Nature 500:168–174.

Higley MJ, Sabatini BL (2012) Calcium signaling in dendritic spines. Cold Spring Harb Perspect Biol 4:a005686.

Hille B (2001) Ion channels of excitable membranes, Ed 3. Sunderland: Sinauer.

Holmes WR (2010) Passive cable modeling. In: Computational modeling methods for neuroscientists (De Schutter E, ed), pp 233–258. Cambridge: MIT Press.

Hsiang JC, Johnson KP, Madisen L, Zeng H, Kerschensteiner D (2017) Local processing in neurites of VGluT3-expressing amacrine cells differentially organizes visual information. Elife 6:e31307.

Hu H, Martina M, Jonas P (2010) Dendritic mechanisms underlying rapid synaptic activation of fast-spiking hippocampal interneurons. Science 327:52–58.

Koch C, Poggio T, Torre V (1982) Retinal ganglion cells: a functional interpretation of dendritic morphology. Phil Trans R Soc Lond B 298:227–264.

Koch C, Rapp M, Segev I (1996) A brief history of time (constants). Cereb Cortex 6:93–101.

Koren D, Grove JCR, Wei W (2017) Cross-compartmental modulation of dendritic signals for retinal direction selectivity. Neuron 95:914–927.

Kothmann WW, Trexler EB, Whitaker CM, Li W, Massey SC, O'Brien J (2012) Nonsynaptic NMDA receptors mediate activity-dependent plasticity of gap junctional coupling in the AII amacrine cell network. J Neurosci 32:6747–6759.

Li W, Trexler EB, Massey SC (2002) Glutamate receptors at rod bipolar ribbon synapses in the rabbit retina. J Comp Neurol 448:230–249.

Lindau M, Neher E (1988) Patch-clamp techniques for time-resolved capacitance measurements in single cells. Pflugers Arch 411:137–146.

Losonczy A, Makara JK, Magee JC (2008) Compartmentalized dendritic plasticity and input feature storage in neurons. Nature 452:436–441.

Major G (2001) Passive cable modeling - a practical introduction. In: Computational neuroscience. Realistic modeling for experimentalists (De Schutter E, ed), pp 209–232. Boca Raton: CRC.

Manookin MB, Beaudoin DL, Ernst ZR, Flagel LJ, Demb JB (2008) Disinhibition combines with excitation to extend the operating range of the OFF visual pathway in daylight. J Neurosci 28:4136–4150.

Marc RE, Anderson JR, Jones BW, Sigulinsky CL, Lauritzen JS (2014) The AII amacrine cell connectome: a dense network hub. Front Neural Circ 8:104.

Masland RH (2012) The tasks of amacrine cells. Vis Neurosci 29:3–9.

Mel BW, Schiller J, Poirazi P (2017) Synaptic plasticity in dendrites: complications and coping strategies. Curr Opin Neurobiol 43:177–186.

Münch TA, da Silveira RA, Siegert S, Viney TJ, Awatramani GB, Roska B (2009) Approach sensitivity in the retina processed by a multifunctional neural circuit. Nat Neurosci 12:1308–1316.

Murphy GJ, Rieke F (2008) Signals and noise in an inhibitory interneuron diverge to control activity in nearby retinal ganglion cells. Nat Neurosci 11:318–326.

Nörenberg A, Hu H, Vida I, Bartos M, Jonas P (2010) Distinct nonuniform cable properties optimize rapid and efficient activation of fast-spiking GABAergic interneurons. Proc Natl Acad Sci USA 107:894–899.

North G, Greenspan RJ (eds) (2007) Invertebrate neurobiology. Cold Spring Harbor: Cold Spring Harbor Laboratory Press.

O'Brien J, Bloomfield SA (2018) Plasticity of retinal gap junctions: roles in synaptic physiology and disease. Annu Rev Vis Sci 4:79–100.

Oltedal L, Hartveit E (2010) Transient release kinetics of rod bipolar cells revealed by capacitance measurement of exocytosis from axon terminals in rat retinal slices. J Physiol 588:1469–1487.

Pang JJ, Abd-El-Barr MM, Gao F, Bramblett DE, Paul DL, Wu SM (2007) Relative contributions of rod and cone bipolar cell inputs to AII amacrine cell light responses in the mouse retina. J Physiol 580:397–410.

Park SJH, Lieberman EE, Ke J-B, Rho N, Ghorbani P, Rahmani P, Jun NY, Lee H-L, Kim I-J, Briggman KL, Demb JB, Singer JH (2020) Connectomic analysis reveals an interneuron with an integral role in the retinal circuit for night vision. Elife 9:e56077.

Peters F, Gennerich A, Czesnik D, Schild D (2000) Low frequency voltage clamp: recording of voltage transients at constant average command voltage. J Neurosci Meth 99:129–135.

Poleg-Polsky A, Ding H, Diamond JS (2018) Functional compartmentalization within starburst amacrine cell dendrites in the retina. Cell Rep 22:2898–2908.

Polsky A, Mel BW, Schiller J (2004) Computational subunits in thin dendrites of pyramidal cells. Nat Neurosci 7:621–627.

Pourcho RG, Goebel DJ (1985) A combined Golgi and autoradiographic study of (^{3}H)glycine-accumulating amacrine cells in the cat retina. J Comp Neurol 233:473–480.

Rall W (1964) Theoretical significance of dendritic trees for neuronal input-output relations. In: Neural theory and modeling (Reiss RF, ed). Palo Alto. Stanford University Press: Reprinted in: The theoretical foundation of dendritic function (Segev I, Rinzel R, Shepherd GM, eds) (1995) pp 122–146. Cambridge, MA: MIT Press.

Ran Y, Huang Z, Baden T, Schubert T, Baayen H, Berens P, Franke K, Euler T (2020) Type-specific dendritic integration in mouse retinal ganglion cells. Nat Commun 11:2101.

Roska B, Werblin F (2001) Vertical interactions across ten parallel, stacked representations in the mammalian retina. Nature 410:583–587.

Schmidt-Hieber C, Jonas P, Bischofberger J (2007) Subthreshold dendritic signal processing and coincidence detection in dentate gyrus granule cells. J Neurosci 27:8430–8441.

Sharpe LT, Stockman A (1999) Rod pathways: the importance of seeing nothing. Trends Neurosci 22:497–504.

Singer JH, Diamond JS (2003) Sustained Ca^{2+} entry elicits transient postsynaptic currents at a retinal ribbon synapse. J Neurosci 23:10923–10933.

Smith RG, Vardi N (1995) Simulation of the AII amacrine cell of mammalian retina: functional consequences of electrical coupling and regenerative membrane properties. Vis Neurosci 12:851–860.

Spruston N, Stuart G, Häusser M (2016) Principles of dendritic integration. In: Dendrites, Ed 3 (Stuart G, Spruston N, Häusser M, eds), pp 351–398. Oxford: Oxford University Press.

Strettoi E, Dacheux RF, Raviola E (1990) Synaptic connections of rod bipolar cells in the inner plexiform layer of the rabbit retina. J Comp Neurol 295:449–466.

Strettoi E, Raviola E, Dacheux RF (1992) Synaptic connections of the narrow-field, bistratified rod amacrine cell (AII) in the rabbit retina. J Comp Neurol 325:152–168.

Strettoi E, Dacheux RF, Raviola E (1994) Cone bipolar cells as interneurons in the rod pathway of the rabbit retina. J Comp Neurol 347:139–149.

Tian M, Jarsky T, Murphy GJ, Rieke F, Singer JH (2010) Voltage-gated Na channels in AII amacrine cells accelerate scotopic light responses mediated by the rod bipolar cell pathway. J Neurosci 30:4650–4659.

Tran-Van-Minh A, Abrahamsson T, Cathala L, DiGregorio DA (2016) Differential dendritic integration of synaptic potentials and calcium in cerebellar interneurons. Neuron 91:837–850.

Tsukamoto Y, Omi N (2013) Functional allocation of synaptic contacts in microcircuits from rods via rod bipolar to AII amacrine cells in the mouse retina. J Comp Neurol 521:3541–3555.

Urban N, Margrie TW (2016) Dendrites as transmitters. In: Dendrites, Ed 3 (Stuart G, Spruston N, Häusser M, eds), pp 603–621. Oxford: Oxford University Press.

Vardi N, Smith RG (1996) The AII amacrine network: coupling can increase correlated activity. Vision Res 36:3743–3757.

Veruki ML, Hartveit E (2002a) AII (rod) amacrine cells form a network of electrically coupled interneurons in the mammalian retina. Neuron 33:935–946.

Veruki ML, Hartveit E (2002b) Electrical synapses mediate signal transmission in the rod pathway of the mammalian retina. J Neurosci 22:10558–10566.

Veruki ML, Mørkve SH, Hartveit E (2003) Functional properties of spontaneous EPSCs and non-NMDA receptors in rod amacrine (AII) cells in the rat retina. J Physiol 549:759–774.

Veruki ML, Mørkve SH, Hartveit E (2006) Activation of a presynaptic glutamate transporter regulates synaptic transmission through electrical signaling. Nat Neurosci 9:1388–1396.

Veruki ML, Zhou Y, Castilho Á, Morgans CW, Hartveit E (2019) Extrasynaptic NMDA receptors on rod pathway amacrine cells: molecular composition, activation, and signaling. J Neurosci 39:627–650.

Vervaeke K, Lörincz A, Nusser Z, Silver RA (2012) Gap junctions compensate for sublinear dendritic integration in an inhibitory network. Science 335:1624–1628.

Weiss J, O'Sullivan GA, Heinze L, Chen H-X, Betz H, Wässle H (2008) Glycinergic input of small-field amacrine cells in the retinas of wildtype and glycine receptor deficient mice. Mol Cell Neurosci 37:40–55.

Werblin FS (2010) Six different roles for crossover inhibition in the retina: correcting the nonlinearities of synaptic transmission. Vis Neurosci 27:1–8.

Williams SR, Stuart GJ (2002) Dependence of EPSP efficacy on synapse location in neocortical pyramidal neurons. Science 295:1907–1910.

Xin D, Bloomfield SA (1999) Comparison of the responses of AII amacrine cells in the dark- and light-adapted rabbit retina. Vis Neurosci 16:653–665.

Yan W, Laboulaye MA, Tran NM, Whitney IE, Benhar I, Sanes JR (2020) Mouse retinal cell atlas: molecular identification of over sixty amacrine cell types. J Neurosci 40:5177–5195.

Yasuda R, Nimchinsky EA, Scheuss V, Pologruto TA, Oertner TG, Sabatini BL, Svoboda K (2004) Imaging calcium concentration dynamics in small neuronal compartments. Sci STKE 2004:pl5.

Zandt B-J, Liu JH, Veruki ML, Hartveit E (2017) AII amacrine cells: quantitative reconstruction and morphometric analysis of electrophysiologically identified cells in live retinal slices imaged with multi-photon excitation microscopy. Brain Struct Funct 222:151–182.

Zandt B-J, Veruki ML, Hartveit E (2018) Electrotonic signal processing in AII amacrine cells: compartmental models and passive membrane properties for a gap junction-coupled retinal neuron. Brain Struct Funct 223:3383–3410.